Research Square

Preprints are preliminary reports that have not undergone peer review.
They should not be considered conclusive, used to inform clinical practice,
or referenced by the media as validated information.

Synergistic Ferroelectric, Ferromagnetic, and Electrochemical Properties of $BaTiO_3$–$CoFe_2O_4$ Nanocomposite for Multifunctional Energy Storage

A. M. Ali
Suez University
Amany E. Harby
Suez University
Khaled Faisal Qasim
Suez University
Ahmed E. Hannora
Suez University
M. M. El-Desoky
mmdesoky@suezuniv.edu.eg
Suez University

Article

Keywords: Multiferroic materials, Ferroelectricity, Ferrimagnetism, Dielectric properties, Energy storage, Pseudocapacitance

Posted Date: September 11th, 2026

DOI: https://doi.org/10.21203/rs.3.rs-10766671/v1

License: This work is licensed under a Creative Commons Attribution 4.0 International License.
Read Full License

Additional Declarations: No competing interests reported.

Synergistic Ferroelectric, Ferromagnetic, and Electrochemical Properties of $BaTiO_3$–$CoFe_2O_4$ Nanocomposite for Multifunctional Energy Storage

A. M. Ali [1], Amany E. Harby,[1] Khaled Faisal Qasim[2] Ahmed E. Hannora[3] and M.M. El-Desoky[1*]

[1]Department of Physics, Faculty of Science, Suez University, Suez, 43518, Egypt

[2] *Department of Science and Engineering Mathematics, Faculty of Petroleum and Mining Engineering, Suez University, Suez, Egypt, 43518.*

[3]Chemistry Department, Faculty of Science, Suez University, Suez, 43518, Egyp

Abstract

$BaTiO_3$–$CoFe_2O_4$ (BTO–CFO) multiferroic nanocomposites were synthesized through a facile co-precipitation route to obtain a multifunctional material with dielectric, magnetic, and electrochemical characteristics relevant to energy-storage technologies. The composite phase's formation was verified via X-ray diffraction (XRD), while the crystallite dimensions derived from the Debye–Scherrer relation were further supported by high-resolution transmission electron microscopy is abbreviated as (HR-TEM). The dielectric characteristics were investigated between 298 and 668 K over the frequency interval of 0.5–1000 kHz. A pronounced ferroelectric phase transition was observed at a Curie temperature of 648 K, demonstrating the intrinsic ferroelectric response of the composite. Analysis of the frequency-dependent exponent, s, indicated that the ac electrical transport is governed predominantly via mechanism called correlated barrier hopping. Polarization–electric field (P–E) characteristics revealed a progressive improvement in energy-storage capability with increasing temperature. The composite exhibited a maximum value for recoverable energy density (W_r) of 6.2 J cm^{-3}, accompanied by 65.9% energy-storage efficiency (η). Room-temperature magnetic measurements performed within an applied field range of −20 to +20 kG confirmed the presence of stable ferromagnetic characteristics, together with appreciable remanent magnetization and coercive field values. Electrochemical characterization further demonstrated a Faradaic pseudocapacitive contribution, yielding a 230 F g^{-1} specific capacitance with a 1 mV s^{-1} scan rate. Furthermore, the electrode maintained 90.3% of its initial capacitance following 1000 consecutive charge–discharge cycles, demonstrating good long-term electrochemical durability. The simultaneous manifestation of ferroelectricity, ferromagnetism, dielectric polarization, and pseudocapacitive behavior highlights the potential of BTO–CFO nanocomposites as multifunctional candidates for advanced energy-storage systems and integrated electronic applications.

Keywords: Multiferroic materials; Ferroelectricity; Ferrimagnetism; Dielectric properties; Energy storage; Pseudocapacitance.

---

*Corresponding author: (M. M. El-Desoky) mmdesoky@suezuniv.edu.eg

1. Introduction

Because magnetic & electric orders can exist in the same phase, multiferroic materials are now of interest [1]. In-depth research is being conducted on this family of materials due to its potential uses in energy storage devices, actuators, sensors, electronic memory devices, spintronic devices, etc. Single-phase & multiphase materials can be used to classify these multiferroic materials [2]. They are anticipated to attain high magnetoelectric coupling at ambient temperature, nanocomposite multiferroic materials made through physically mixing ferroelectric & ferromagnetic materials have received a lot of concentrated effort in the last ten years [3, 4]. This coupling allows an electric field to directly affect magnetization and vice versa. The selection of the ferroelectric & ferromagnetic phases plays a substantial role in achieving an effective magnetoelectric conversion output as well as a desired operating temperature (Curie temperature > Room temperature). $BaTiO_3$ is a prominent ferroelectric material having a high dielectric constant, an adjustable Curie temperature, better chemical stability, low dielectric tangent loss, high spontaneous polarization as well as environmental friendliness [4]. Nanocomposite multiferroic systems based on $BaTiO_3$ have been created and investigated in the literature. Spinel ferrites & garnet ferrites are the two main types of cubic ferrites. The family of spinel-ferrites includes cobalt ferrite ($CoFe_2O_4$). Because of its high coercivity and magnetization, this hard magnetic material (CFO) may be used in nanocomposite multiferroic heterostructures, spintronics devices and magnetic recording applications [5]. Cobalt ferrite ($CoFe_2O_4$) is regarded as an extremely important magnetic phase because of its high values of coercive field (~0.5 T) & saturation magnetization (~80 emu/g) [6]. Cobalt ferrite has a high magnetostriction and is ferrimagnetic. $BaTiO_3$– $CoFe_2O_4$ nanocomposites combine the ferrimagnetism of $CoFe_2O_4$ with the ferroelectricity of $BaTiO_3$. Since it was initially discovered in 1972, $CoFe_2O_4$ & $BaTiO_3$ nanocomposites have been developed and manufactured using a variety of novel techniques, including spark plasma sintering [7], microwave-assisted sol-gel [8], sol-gel routes [9] and microwave hydrothermal method [10]. Also, investigations have examined how the ratio of the ferromagnetic $CoFe_2O_4$ phase to the ferroelectric $BaTiO_3$ phase affects the structural, dielectric, ferroelectric, and also magnetic characteristics of nanocomposites. Chaudhuri et al. [11] observed a notable improvement in magnetic, dielectric along with magnetoelectric characteristics of core-shell $CoFe_2O_4$:$BaTiO_3$ nanocomposites compared to a sample with a mixed structure. Also, Duong et al. [12] found that when compared to comparable

types of nanocomposites with $BaTiO_3$ in the core as well as layered structures, core-shell structured $CoFe_2O_4$-$BaTiO_3$ nanocomposites with $CoFe_2O_4$ in the core had the highest magnetoelectric coefficient value. Gao et al. [13] found that reducing the core size significantly improved the ferroelectric, magnetic and magnetoelectric characteristics of the $CoFe_2O_4$-$BaTiO_3$ core-shell structured nanocomposite. Zheng et al. [14] produced an artificial multiferroic made of $BaTiO_3$-$CoFe_2O_4$ nanostructures, and a reduction in magnetism at the Curie temperature was thought to be proof of magnetoelectric coupling. A number of transition metal oxides, including V_2O_5, Co_3O_4, Fe_2O_3, $CoFe_2O_4$ and WO_3 have been extensively used to increase the pseudocapacitance of supercapacitors. Specifically, $CoFe_2O_4$ has a huge theoretical capacitance of about 916 mAh/g and contains the Co (II) along with Fe (III) elements many times in the tetrahedral as well as octahedral locations [15]. Investigate the combined ferroelectric, ferromagnetic, and electrochemical properties of $CoFe_2O_4$–$BaTiO_3$ nanocomposites. While this system has been widely studied for its multiferroic behavior arising from a coupling between the ferroelectric $BaTiO_3$ phase along with the ferromagnetic $CoFe_2O_4$ phase most studies primarily focus on magnetoelectric coupling.

In contrast, the electrochemical performance of such nanocomposites, particularly in conjunction with their multiferroic properties, remains largely unexplored. In this context, the purpose of this investigation work is to present a comprehensive investigation for the structural, electrochemical behavior alongside the ferroelectric and ferromagnetic properties for $CoFe_2O_4$–$BaTiO_3$ nanocomposites synthesized via the coprecipitation method, with the goal of understanding their combined multifunctional performance.

2. Experimental

2.1 Materials

$CoCl_2.6H_2O$, $Fe(NO_3)_3.9H_2O$, NH_4OH were purchased from Alfa-Chemika (99.9) as well as utilized as received, without additional purification. Deionized (DI) water was commonly utilized as the primary solvent throughout the synthesis.

2.2 Synthesis of $CoFe_2O_4$+$BaTiO_3$ Nanoparticles

Stoichiometric amounts of $CoCl_2.6H_2O$, as well as $Fe(NO_3)_3.9H_2O$ were dissolved in DI water in a 1:2 molar ratio to maintain the target spinel cation balance. The solution was continuously

stirred at temperature 80 °C for 2h to promote homogeneous metal-citrate complexation. The mixture's pH was systematically adjusted to 8 by the dropwise addition of aqueous ammonia to optimize the premature precipitation.

Following neutralization, the solution was subjected to heating at 80 °C with continuous magnetic stirring to evaporate excess water. As dehydration progressed, the liquid transitioned into a highly viscous, translucent brown gel. Gel was dried at 80°C for 4h to obtain the resultant powder as a dark and fluffy. Then $BaTiO_3$ was added with $CoFe_2O_4$ ($Co(OH)_2$:$Fe(OH)_3$:$BaTiO_3$ in a 1:2:1 molar ratio). The calcination was performed at 800 °C using a muffle furnace for 1h to induce highly crystalline spinel phase formation. Hereafter, the $CoFe_2O_4$–$BaTiO_3$ composite will be referred to as BTO-CFO for simplicity and consistency throughout the manuscript.

2.3. Characterization

An Xray diffraction (Rigaku MiniFlex 600 diffractometers) examination was carried out on the sample using wavelength, λ (Cu-Kα ra-diation) = 1.5418 Å. Our samples were analyzed for particle size and structure using high-resolution transmission electron microscope instrument ((JEM-2100 TEM instrument) is abbreviated as HR-TEM. The sample was evaluated by electrical and dielectric testing with frequencies ranging from 0.5 to 1000 kHz and temperatures varying from 298 to 668 K. A Microtest 6377 LCR meter instrument was used to measure dielectric properties. The Sawyer-Tower circuit operates at 50 Hz to detect the sample's ferroelectric hysteresis loop. Magnetization-magnetic field hysteresis loop was evaluated utilizing a vibrating-sample magnetometer instrument (VSM Lake Shore model 7410). Electrodes were synthesized by mixing a paste consisting of the materials under examination, acetylene black, & polyvinylidene fluoride, PVDF with a mass ratio of 75:15:10, with ethanol as the solvent. This paste was then applied to FTO glass substrate. The electrodes were subsequently dried at 80°C for 2h to remove the solvent. The materials' electrochemical properties were evaluated via Galvanostatic charge-discharge, GCD along with cyclic voltammetry (CV) techniques, with a potentiostat. Electrochemical impedance spectroscopy technique, EIS was performed using a Biologic SP-1500 at a constant potential of 10 mV, covering a frequency range from 10^{-1} - 10^5 Hz. Three electrodes were used for all electrochemical measurements, where the prepared active material on FTO glass served as a working electrode, a platinum sheet (2 cm^2) acted as a counter electrode, as well as a saturated calomel electrode, SCE was utilized as a reference electrode. The CV was carried out at scan

rates of 1-100 mV/s within a potential of -0.1 - +0.9 V, while GCD was implemented at current densities of 1-10 A/g. All experiments were implemented in a 1 M H_2SO_4 aqueous electrolyte solution**.**

3. Results Analysis

3.1. Structural characterization

Fig. 1 displays the BTO-CFO sample's X-ray diffraction (XRD) observed pattern. $BaCoFe_6O_{11}$ (JCPDS 01-084-1857), BaO_2 (JCPDS 00-007-0233), $CoFe_2O_4$ (JCPDS 00-022-1086), and $Ba_4Ti_2O_{27}$ (JCPDS 00-004-0013) are the 4 phases that were found. The structure of $BaCoFe_6O_{11}$ has rhombohedral structure for space group R-3m, BaO_2 has tetragonal structure for space group I4/mmm, $CoFe_2O_4$ has Cubic structure for space group Fd3m as well as $Ba_4Ti_2O_{27}$ has Monoclinic structure of space group C2/m. The following Scherrer's equation was utilized to get average nano-crystallite size [16]:

$$D = \frac{\kappa \lambda}{\beta \cos\theta} \quad (1)$$

In this equation, K (which has a value of 0.89) denotes the correction factor, D denotes an average nano-crystallite size, β symbolizes the width of the peak (half-maximum full width), λ (nm, CuKα radiation) symbolizes X-ray wavelength & θ symbolizes the Bragg angle. The value of D was 24.4 nm. δ symbolizes dislocation density, could be calculated applying the formula below [17]:

$$\delta = \frac{1}{D^2} \quad (2)$$

Additionally, the lattice strain, ε could be calculated through the formula below [18]:

$$\varepsilon = \frac{\beta}{4\ tan\theta} \quad (3)$$

The calculated lattice strain (ε) is 9.1×10^{-3}, indicating a relative low lattice distortion in the crystal structure. The dislocation density (δ) is 3.5×10^{-5} nm^{-2}, suggesting a moderate density of crystal defects. More thorough information on the structure of the sample was further gained via the HR-TEM examination. Fig. 2 illustrates the HR-TEM images of the BTO-CFO sample. In Fig. 2(a), the particles displayed an irregular form. Using a Gaussian fit, the observed particle size is approximately 24.6 nm, and the particle size distribution histogram of the BTO-CFO sample is shown in Fig. 2(b). Fig. 2(c) shows lattice fringes that have an interplanar d-spacing of

0.24 nm corresponding to the (024) plane of $BaCoFe_6O_{11}$ phase. Selected Area Electron Diffraction, abbreviated as SAED pattern which exhibits distinct diffraction spots (as shown in Fig. 2(d)), and confirming highly crystalline nature for the BTO-CFO nanoparticles. The positions of the diffraction spots roughly correspond to 0.24 nm, corresponding to the (024) plane of $BaCoFe_6O_{11}$ phase. The HR-TEM & XRD data are compatible. The high crystallinity confirmed by HR-TEM and SAED provides a structural basis for the enhanced ferroelectric and ferromagnetic properties discussed in the subsequent sections, since well-crystallized grains generally facilitate polarization and magnetic domain formation.

3.2. Dielectric and AC conductance studies

For the sample of BTO-CFO at different frequencies, Fig. 3 (a and b) illustrates how real part ε′ and also Imaginary part ε" for dielectric constant varies with temperature, respectively. The typical behavior of ferroelectrics was suggested by the observation of a structural phase transition for a temperature. Near the high-temperature region, ε′ exhibits a rapid increase, indicating the ferroelectric–paraelectric phase transition's onset associated with the Curie temperature (T_C= 648 K). Notably, according to Fig. 3(a), ε′ values exceed 10^3, confirming the significant enhancement in dielectric properties of the studied system. Materials with high dielectric constant are highly relevant to energy storage and electronic applications, as the stored energy density is directly proportional to the ε′. Increasing ε′ leads to enhanced capacitance [19]. Fig. 3(b), ε" exhibits a well-defined peak at nearly the same temperature for all investigated frequencies. Therefore, the frequency-independent peak can be considered a characteristic signature of the ferroelectric phase transition.

The ferroelectric response observed in the BTO–CFO nanocomposite can be associated with its complex multiphase constitution, as revealed by X-ray diffraction analysis. The identified crystalline constituents comprise rhombohedral $BaCoFe_6O_{11}$, cubic $CoFe_2O_4$, monoclinic $Ba_4Ti_2O_{27}$, together with a small fraction of tetragonal BaO_2. Among these phases, the Ti-bearing constituent is expected to contribute significantly to dielectric polarization owing to the displacement of Ti ions relative to the surrounding oxygen framework. In addition, $CoFe_2O_4$ and $BaCoFe_6O_{11}$ can modify the overall ferroelectric response through interfacial coupling and strain generated between the different crystalline phases. Previous investigations of $BaTiO_3$–$CoFe_2O_4$-

based composites have likewise demonstrated that the incorporation of the ferrimagnetic $CoFe_2O_4$ phase does not necessarily suppress the ferroelectric response [20–22]. The pronounced dielectric feature centered near 648 K is owing to the transition from the ferroelectric state into the paraelectric state. Rather than exhibiting an ideally sharp transition, the dielectric anomaly extends over a relatively broad temperature interval. Such behavior can reasonably be related to the compositional and structural heterogeneity of the multiphase system, together with interfacial stress and variations in the local atomic environment. These factors can produce a distribution of transition temperatures throughout the composite. Furthermore, the observed dependence of dielectric properties on frequency suggests a contribution from the dynamic behavior of ferroelectric domain walls. Their capability to follow the externally applied electric field progressively decreases as the measurement frequency increases, thereby contributing to the frequency-dependent dielectric behavior.

Fig. 4 shows the ε′ vs. frequency (f) of BTO-CFO, throughout an over the temperature interval of 298–663 K. Dielectric materials often exhibit a significant a decline in ε′ as frequency increases [23]. The significant reduction in ε′ with increasing frequency, at higher frequencies, charge carriers as well as dipoles cannot adequately respond to the swift changes in the applied electric field. In the low frequency spectrum, space charge and interfacial polarization contribute significantly to the dielectric response, resulting in high ε′ values. However, with a rise in frequency, these polarization processes progressively lag behind the applied field, causing a marked decrease in the dielectric constant [24-26]. The following formula (Jonscher's law) shows that the AC conductivity, σ_{ac}, for semiconductors rises with frequency [27]:

$$\sigma_{ac} = \sigma_{dc} + A\omega^{S} \quad (4)$$

Where σ_{dc} as well as σ_{ac} represent the DC as well as AC conductivity, respectively, s ($0 \leq s \leq$)) is referred to as the frequency exponent, ω represents angular frequency and also A is a constant (as the polarizability force). Fig. 5 illustrates how the σ_{ac}, depends on the frequency of BTO-CFO sample at various temperatures. The findings reveal that σ_{ac} increases at all temperature with frequency. σ_{ac} rises with frequency, possibly due to electrons and atoms actively moving and hopping between equilibrium locations. σ_{ac} exhibits universal power law behavior, often termed as Jonscher's law [28]. The slopes of plots (ln σ_{ac} vs. ln f) determine the values of s at

various temperatures. The temperature-dependent parameter s for the tested sample is displayed in the inset figure; it clearly decreases with increasing temperature. The results obtained correspond with correlated barrier hopping (CBH) model [29].

3.3. Ferroelectric studies

Fig. 6 presents the polarization–electric field, (P–E) hysteresis loops for the BTO-CFO sample at room temperature, with the applied voltages varied up to 220 volt, as well as at a frequency = 50 Hz. The ferroelectric behavior of the BTO-CFO sample is evidenced by the observed increase in remnant polarization (P_r) as the applied E increases [30]. Fig. 7 illustrates the P–E hysteresis loops under varying temperatures for the BTO-CFO sample measured at a f = 50 Hz & an applied voltage = 220 volt. With increasing temperature, the remnant polarization, P_r along with coercive field (E_c) gradually decreases due to enhanced thermal fluctuations, which disrupt the alignment of ferroelectric domains and reduce their stability. The increased thermal energy facilitates domain wall motion, making polarization switching easier under lower applied electric fields. Consequently, the P–E hysteresis loops become narrower [31-33]. As exhibited in Fig. 8(a), As temperature rises, P-E loops become narrower, resulting in decreased P_{max} (maximal polarization), P_r, and E_c, this is due to the loss of ferroelectric domains [34]. The number of switchable domains, often corresponds with the value of P_{max}. Furthermore, the volume of the backswitched domain is proportionate to the P_{max}-P_r value. When a suitable voltage is provided, the polarization of the ferroelectrics approaches P_{max}. Following the removal of the voltage that was applied, the polarization reaches P_r. The switching polarization can partially reverse during the relaxing process. This behavior is called polarization backswitching, and P_{max}-P_r may be used to describe the related backswitching polarization (P_{bc}) [35]. The backswitching polarization (P_{bc}) increases with temperature (as seen in Fig. 8(b)). The increase in the difference between P_{max} and P_r with increasing temperature is associated with the thermally activated movement of domain-walls. Higher temperature enhances the mobility of ferroelectric domains, allowing a larger number for domains to align with the applied electric field, which increases P_{max}. However, after removing the electric field, part of these domains returns to energetically favorable orientations due to thermal fluctuations, resulting in a comparatively smaller increase in P_r. Consequently, the value of (P_{max}-P_r) increases with temperature [36]. This behavior indicates an enhancement in the reversible polarization component, which is beneficial for both ferroelectric switching and charge–discharge processes in energy-storage applications. Also, the

increased (P_{max}-P_r) value suggests a higher recoverable polarization, which is desirable for energy-storage devices because a larger fraction of the stored electrical energy can be released throughout the discharge process [37]. The Arrhenius law corresponds with the relationship between P_{max}, P_r, & T in high field [33, 35]:

$$P_{max} - P_r = P_\circ \exp\left(-\frac{E_{DS}}{K_B T}\right) \quad (5)$$

where E_{DS} refers to activation energy for domain switching, K_B refers to Boltzmann's constant, and $P_\circ$ refers to constant. A slope of ln (P_{max} - P_r) versus 1/T can be employed to estimate the E_{DS}. The Arrhenius curve for the BTO-CFO sample at different temperatures is shown in Fig. 8(c). E_{DS} generally depends on the electric field that is applied. The E_{DS} value was determined to be 0.019 eV.

The energy storage characteristics of dielectric capacitors, such as W_r (refers to energy storage density), in addition to η (refers to energy storage efficiency), and W_L (refers to energy loss) can be estimated using (P–E) hysteresis loops' integral. Their equations are described as follows [38]:

$$W_r = \int_{P_r}^{P_{max}} E \, dP \quad (6)$$

$$\eta = \left(\frac{W_r}{W_r + W_L}\right) \times 100 \quad (7)$$

Fig. 9(a) displays the schematic depiction for the P–E hysteresis loop. The variation of the hysteresis loop area, ⟨A⟩, with temperature is demonstrated in Fig. 9(b). The loop area declines as the temperature rises at an applied voltage = 220 volt. Irreversible domain wall motion has been related to the loop area, and a bigger loop area at a reduced temperature suggests that domain-wall motion is increasingly hindered as the temperature decreases [35]. The W_r & η for the BTO-CFO sample between temperature ranges 298 – 423 K are demonstrated in Fig. 9(c). W_r & η exhibited progressively increasing values at elevated temperatures, reaching 6.2 J/cm^3 and 65.9%, respectively. As a result, we believe the BTO-CFO sample is a suitable option for capacitive energy storage applications.

The structural characteristics identified by XRD offer a reasonable explanation for the observed dielectric and ferroelectric response. In particular, the $Ba_4Ti_2O_{27}$ phase contains Ti–O structural units that may facilitate ionic displacement and, consequently, contribute to the development of

electric polarization. Meanwhile, the incorporation of $CoFe_2O_4$ and $BaCoFe_6O_{11}$ introduces ferrimagnetic constituents into the composite, resulting in considerable structural inhomogeneity and strain at the interfaces between the coexisting phases. These interfacial regions can generate localized electric fields and influence the mobility of ferroelectric domain walls. As a result, the ferroelectric phase transition may occur over a broader temperature interval instead of displaying the sharp transition generally associated with a structurally uniform ferroelectric phase. The small fraction of BaO_2 detected in the XRD pattern could also be related to defect-induced polarization; however, its specific influence on ferroelectric switching cannot be determined conclusively from XRD data alone [20–22].

3.4.Ferromagnetic properties

The hysteresis behavior of magnetization M with respect to magnetic field (H) at room temperature are traced to determine the ferromagnetic characteristics of the BTO-CFO, acquired by applying a field of up to ±20000 G as shown in Fig. 10. As can be observed the BTO-CFO sample exhibits a typical ferrimagnetic behavior that includes a coercive field of H_c = 1160.9 G, remanent magnetization of M_r = 2.99 emu/g & saturation magnetization of M_s = 7.81 emu/g. The ferromagnetic behavior of the $BaTiO_3$–$CoFe_2O_4$ nanocomposite originates from the ferrimagnetic $CoFe_2O_4$ phase embedded in the non-magnetic $BaTiO_3$ matrix. The saturation magnetization (M_s = 7.81 emu/g) confirms the contribution of $CoFe_2O_4$ to the magnetic response, while its relatively low value is owing to the dilution effect of $CoFe_2O_4$ (magnetic phase) with $BaTiO_3$ (non-magnetic phase) [6, 39]. The remanent magnetization (M_r = 2.99 emu/g) indicates the ability of the nanocomposite to retain magnetization after removal of the external field. The obtained squareness ratio (M_r/M_s = 0.383) falls within the range commonly reported for $CoFe_2O_4$ nanoparticles (≈0.3–0.5) [40, 41]. Such a value indicates appreciable magnetic anisotropy and stable magnetic domains, confirming the hard ferrimagnetic nature of the $CoFe_2O_4$ phase [42, 43]. Furthermore, the high coercivity (H_c = 1160.9 G) reflects the strong magnetocrystalline anisotropy and domain wall pinning associated with the $CoFe_2O_4$ phase [40].

The magnetic response obtained from the M–H hysteresis measurement is consistent with the multiphase nature of the material established by XRD analysis. Among the detected constituents, cubic $CoFe_2O_4$ with the Fd-3m space group is expected to make the dominant contribution to

magnetization because of its spinel framework containing magnetically ordered Co and Fe ions. The rhombohedral $BaCoFe_6O_{11}$ phase (R-3m) may provide an additional magnetic contribution owing to the presence of transition-metal ions within its crystal structure. By comparison, $Ba_4Ti_2O_{27}$ with monoclinic C2/m symmetry and BaO_2 with tetragonal I4/mmm symmetry are expected to have only a limited influence on the net magnetic moment. Accordingly, the measured hysteresis behavior can be rationalized by the coexistence of the magnetic $CoFe_2O_4$ and $BaCoFe_6O_{11}$ constituents within a matrix containing comparatively weakly or nonmagnetic Ti- and Ba-based phases.

The agreement between the structural and magnetic observations supports the formation of a multiphase magnetoelectric system. Furthermore, the measured magnetic characteristics, including the retained remanent magnetization and stable hysteresis response, indicate satisfactory magnetic stability. These features, together with the dielectric and ferroelectric characteristics, make the BTO–CFO composite an attractive candidate for multifunctional electronic components and advanced energy-storage technologies.

3.5.Electrochemical Studies

The CV curves of BTO-CFO sample recorded over scan rates of 1 - 100 mV/s as demonstrated in Fig. 11(a).

Using cyclic voltammetry, the specific capacitance of BTO-CFO sample was obtained using the equation given below [44]:

$$C_S = \frac{1}{2msΔV} \int I.dV \quad (8)$$

where m refers to the active material mass, s refers to scan rate, ∫ I.dV refers to the area under the CV curve (representing the total accumulated charge retained by the electrode [45]) and ΔV refers to voltage window. The sample shows Cs reaches 230 F/g at scan rate 1 mV/s. The CV curves display broad redox peaks, indicative of Faradaic pseudocapacitive behavior [46, 47]. Reversible redox reactions for the Co^{2+}/Co^{3+} as well as Fe^{2+}/Fe^{3+} species in $CoFe_2O_4$ are responsible for these redox transitions. Additionally, the following equations can be used to represent the surface-controlled as well as diffusion-controlled components that make up the capacitor's capacitive performance [49 ,48]:

$$I = a\, \nu^{b} \quad (9)$$

$$\log I = \log a + b \log v \quad (10)$$

where I (A) symbolizes the current, a symbolizes the proportionality constant, v (mV/s) symbolizes the scan rate b symbolizes the power exponent. The b value assists in the analysis of the charge-storage mechanisms: surface capacitance predominates as b approaches 1, while diffusion control governs when b is around 0.5. Therefore, a & b values of 0.5 or 1 show whether the system operates as a capacitive or battery-type system [50, 51]. Here, both a & b are the constants that were determined using the log i vs. log v direct curve (Fig. 11(b)). The estimated b value from Fig. 11(b) is 0.65, which means that BTO-CFO sample possesses both capacitive as well as diffusive control phenomena.

Fig. 12(a) displays the supercapacitor's GCD curves at different current densities. Using following formula, the supercapacitor's Cs was computed from the GCD discharge curve [52]:

$$C_s = \frac{I\,\Delta t}{m\,\Delta V} \quad (11)$$

where I stand for current in (A) and Δt for discharge duration (s). The values of Cs (as shown in Fig. 12(b)) are 288.8, 286.6, 222.2 and 211.1 F/g, at 1, 2, 5 as well as 10 A/g, respectively. The following formulas are used to determine the energy density (E_s) and aslo power density (P_s) [53]:

$$E_s = \frac{C_s \Delta V^2}{7.2} \quad (12)$$

$$P_s = \frac{E_s x 3600}{\Delta t} \quad (13)$$

Fig. 12(c) displays the E_s and P_s behaviors of BTO-CFO sample across various current densities. E_s usually decreases as current density increases because the system discharges energy more quickly, which reduces total charge storage. On the other hand, power density often increases with current density, indicating the system's faster energy supply [49]. The results we obtained are similar to those reported in the literature. The device based on $CoFe_2O_4$/MWCNT has a maximum specific capacitance = 98 Fg^{-1} at 1 $mA.cm^{-2}$, with energy and aslo power densities of 26.67 Wh/kg & 319 W/kg [54], respectively. Our sample reveals the maximum Cs of 288.8 F/g & E_s of 32.1 Wh/kg at current density 1A/g. Cycling stability (Fig. 12(d)) over 1000 GCD cycles

at 1A/g demonstrated excellent capacitance retention of 90.3%, it shows that the cyclic stability is good. Electrochemical impedance spectroscopy is abbreviated as EIS was performed to investigate the electrochemical behavior of the prepared sample (as shown in Fig. 13). Analysis was done on the impedance spectra utilizing an equivalent circuit model composed of $R_o+(R_1||CPE_1)+(R_2||CPE_2)$, where R_o represents solution resistance, R_1 as well as R_2 correspond to bulk resistance and resistance of the grain boundary, respectively [55], while the CPE elements reflect non-ideal capacitive characteristics resulting from surface heterogeneity and porous electrode characteristic (which C was replaced by CPE). The fitted parameters were listed in table. 1. Overall, the fitted impedance parameters prove that the electrode possesses favorable electrochemical characteristics for high-performance supercapacitor applications.

Overall, the experimental findings demonstrate a clear relationship between the multiphase architecture of the BTO–CFO composite and its diverse functional responses. XRD characterization revealed the coexistence of rhombohedral $BaCoFe_6O_{11}$, cubic $CoFe_2O_4$, monoclinic $Ba_4Ti_2O_{27}$, and tetragonal BaO_2 phases, while the HR-TEM results provided complementary evidence for the nanocrystalline character of the material. The coexistence of these phases generates a large number of interphase boundaries and defect-associated sites, which can strongly influence polarization processes and charge migration within the composite. The Ti-containing constituent is expected to make an important contribution to the dielectric response, resulting in a relative permittivity exceeding 10^3 and a pronounced dielectric feature near $T_C \approx 648$ K. This anomaly is consistent with a ferroelectric-to-paraelectric transition and is further supported by the corresponding P–E hysteresis characteristics. On the magnetic side, the $CoFe_2O_4$ and $BaCoFe_6O_{11}$ constituents are primarily responsible for the measured magnetization because of their magnetically active Co–Fe sublattices. Their contribution is clearly reflected in the M–H hysteresis behavior. Therefore, the simultaneous presence of electrically polarizable Ti-based phases and magnetically active Co–Fe oxide phases establishes the structural basis for the coexistence of ferroelectric and magnetic functionalities. The heterogeneous interfaces formed between the different constituents can also provide favorable pathways for ionic/electronic transport and facilitate reversible Faradaic reactions during electrochemical operation. Accordingly, the composite exhibits pronounced pseudocapacitive characteristics, delivering a specific capacitance of 288.8 F g^{-1} at 1 A g^{-1} and maintaining 211.1 F g^{-1} when the current density is increased to 10 A g^{-1}, demonstrating satisfactory rate performance. In addition, 90.3%

for the initial capacitance remains after 1000 galvanostatic charge–discharge cycles, indicating good electrochemical durability. The multifunctional behavior of BTO–CFO can therefore be attributed to the synergistic contribution of its nanocrystalline multiphase architecture, interfacial effects, dielectric polarization, ferroelectric switching, magnetic ordering, and reversible electrochemical charge storage [56-61]. The combination of these properties makes this composite a promising choice for advanced energy-storage devices, supercapacitor electrodes, and multifunctional electronic systems.

3.6.Comparison of Structural, Multiferroic, and Energy-Storage Properties with Previous Reports

The multifunctional performance of the current BTO-CFO composite was compared with earlier $BaTiO_3$-$CoFe_2O_4$ systems (Table. 2). Previous research mainly looked at the coexistence and connection of ferroelectric $BaTiO_3$ and ferrimagnetic $CoFe_2O_4$ phases. Zheng et al.[56] were the first to show nanoscale ferroelectric-magnetic coupling in BTO-CFO nanostructures, highlighting the potential of this system for multifunctional devices. Shankar et al.[57] later reported a recoverable energy density = 8.33 mJ cm^{-3} with an efficiency = 59.7% for a BT-5CFO composite, along with a magnetoelectric coefficient = 13.33 mV cm^{-1} Oe^{-1}. Other studies have demonstrated that increasing the CFO content typically improves the magnetic response but might decrease the dielectric and aslo ferroelectric properties owing to higher leakage and the dilution of the ferroelectric phase [58-60]. Recently, Soleimani et al. [21] reported a dielectric constant of around 2018 and a remanent polarization of about 10 μC cm^{-2} for a BTO-CFO composite with 7.5 wt% CFO. Yoon et al.[61] confirmed that BTO-CFO ceramics exhibit both ferroelectric and magnetic responses. Compared to these findings, the current composite shows a wider range of functionalities. It combines a high dielectric constant of over 10^3, a ferroelectric transition at about 648 K, room-temperature ferroelectric and magnetic hysteresis, and pseudocapacitive energy storage. The specific capacitance of 288.8 F/g at 1 A/g as well as capacitance retention of 90.3% after 1000 GCD cycles demonstrate an electrochemical energy-storage capability that most previous BTO-CFO studies have not addressed. These results emphasize the potential of this multiphase composite as a multifunctional material for integrated dielectric, magnetoelectric, and electrochemical energy-storage applications.

Conclusion

A nanocrystalline $CoFe_2O_4$–$BaTiO_3$ composite containing two distinct phases was prepared through a straightforward co-precipitation route. Comprehensive structural and functional characterization demonstrated the coexistence of dielectric, ferroelectric, ferromagnetic, and electrochemical responses within the synthesized material. X-ray diffraction together with HR-TEM verified the development of the nanostructured composite and its well-defined crystalline constituents. Temperature-dependent dielectric measurements revealed a distinct transition near 648 K, associated with the ferroelectric-to-paraelectric transformation, while the dielectric constant reached values above 10^3. The P–E & M–H hysteresis characteristics evaluated at room temperature provided direct evidence of the simultaneous electric polarization and magnetic ordering, highlighting the multifunctional nature of the composite. The electrochemical response was also strongly dependent on the applied current density. Specific capacitances of 288.8, 286.6, 222.2, and 211.1 F g^{-1} were obtained at 1, 2, 5, and 10 A g^{-1}, respectively, demonstrating a substantial pseudocapacitive contribution together with acceptable rate performance. In prolonged galvanostatic charge–discharge testing, 90.3% for the initial capacitance was preserved after 1000 cycles, confirming the material's favorable cycling durability. Taken together, the combination of high dielectric polarization, ferroelectric switching, magnetic functionality, and reversible pseudocapacitive charge storage demonstrates the considerable potential of $CoFe_2O_4$–$BaTiO_3$ as a multifunctional material for next-generation energy-storage systems, particularly high-performance supercapacitor technologies.

Funding: This research received no specific grant from any funding agency in the public or commercial.

Data Availability: The datasets generated and/or analyzed during the current study are available from the corresponding author upon reasonable request.

References

[1] M.M. Selvi, P. Manimuthu, K.S. Kumar, C. Venkateswaran, Magnetodielectric properties of $CoFe_2O_4$–$BaTiO_3$ core–shell nanocomposite, Journal of magnetism and magnetic materials 369 (2014) 155-161.

[2] N. Adhlakha, K. Yadav, R. Singh, Effect of $BaTiO_3$ addition on structural, multiferroic and magneto-dielectric properties of 0.3 $CoFe_2O_4$− 0.7 $BiFeO_3$ ceramics, Smart materials and structures 23(10) (2014) 105024.

[3] H.-f. Zhang, S.W. Or, H.L.W. Chan, Electrical, magnetic, and magnetoelectric characterization of fine-grained Pb ($Zr_{0.53}Ti_{0.47}$) O_3–($Ni_{0.5}Zn_{0.5}$) Fe_2O_4 composite ceramics, Journal of alloys and compounds 509(21) (2011) 6311-6316.

[4] Z. Wang, R. Gao, G. Chen, X. Deng, W. Cai, C. Fu, Dielectric, ferroelectric and magnetoelectric properties of in-situ synthesized $CoFe_2O_4$/$BaTiO_3$ composite ceramics, Ceramics International 46(7) (2020) 9154-9160.

[5] S.A. Raza, S.U. Awan, S. Hussain, S.A. Shah, A.M. Iqbal, S. Khurshid Hasanain, Structural, ferromagnetic, electrical, and dielectric relaxor properties of $BaTiO_3$ and $CoFe_2O_4$ bulk, nanoparticles, and nanocomposites materials for electronic devices, Journal of Applied Physics 128(12) (2020).

[6] M. Atif, R. Sato Turtelli, R. Grossinger, F. Kubel, Influence of manganese substitution on the microstructure and magnetostrictive properties of Co1− xMnxFe_2O_4 (x= 0.0–0.4) ferrite, Journal of Applied Physics 113(15) (2013).

[7] Y. Liu, G. Xu, Y. Xie, H. Lv, C. Huang, Y. Chen, Z. Tong, J. Shi, R. Xiong, Magnetoelectric behaviors in $BaTiO_3$/$CoFe_2O_4$/$BaTiO_3$ laminated ceramic composites prepared by spark plasma sintering, Ceramics International 44(8) (2018) 9649-9655.

[8] W. Yang, Z. Wang, T. Wang, M. Jin, J. Xu, Y. Sui, Ferroelectric and magnetic properties of $CoFe_2O_4$/$BaTiO_3$ prepared by microwave-assisted sol-gel method, Journal of Superconductivity and Novel Magnetism 30(2) (2017) 539-543.

[9] A.S. Gaikwad, S.E. Shirsath, S.R. Wadgane, R. Kadam, J. Shah, R. Kotnala, A. Kadam, Magneto-electric coupling and improved dielectric constant of BaTiO3 and Fe-rich ($Co_{0.7}Fe_{2.3}O_4$) ferrite nano-composites, Journal of Magnetism and Magnetic Materials 465 (2018) 508-514.

[10] T. Ramesh, V. Rajendar, S. Murthy, $CoFe_2O_4$–$BaTiO_3$ multiferroic composites: role of ferrite and ferroelectric phases on the structural, magneto dielectric properties, Journal of Materials Science: Materials in Electronics 28(16) (2017) 11779-11788.

[11] A. Chaudhuri, K. Mandal, Large magnetoelectric properties in $CoFe_2O_4$: $BaTiO_3$ core–shell nanocomposites, Journal of Magnetism and Magnetic Materials 377 (2015) 441-445.

[12] G.V. Duong, R. Grössinger, R.S. Turtelli, Effect of structure on magnetoelectric properties of $CoFe_2O_4$–$BaTiO_3$ multiferroic composites, Journal of Magnetism and Magnetic Materials 310(2) (2007) e361-e363.

[13] R. Gao, Z. Wang, G. Chen, X. Deng, W. Cai, C. Fu, Influence of core size on the multiferroic properties of $CoFe_2O_4$@ $BaTiO_3$ core shell structured composites, Ceramics International 44 (2018) S84-S87.

[14] H. Zheng, J. Wang, S. Lofland, Z. Ma, L. Mohaddes-Ardabili, T. Zhao, L. Salamanca-Riba, S. Shinde, S. Ogale, F. Bai, Multiferroic batio3-cofe2o4 nanostructures, Science 303(5658) (2004) 661-663.

[15] Q. Qu, Z. Chen, G.-T. Sun, L. Qiu, M.-Q. Zhu, $CoFe_2O_4$ nanoparticles as a bifunctional agent on activated porous carbon for battery-type asymmetrical supercapacitor, Chemical Synthesis 4(2) (2024) N/A-N/A.

[16] M. Shafeeq, A.M. Qureshi, S.R. Ejaz, N. Farooq, A.H. Syeda, H. Riaz, W. Iman, K. Qamar, M.I. Khan, A. Shanableh, Metal-substituted ferrites as efficient photocatalysts for the removal of crystal violet from wastewater, Polyhedron (2026) 117986.

[17] S.S. Abdul-Jabbar, K.H. Harbi, A Study of the Relationship between the Two Types of Crystallite Dislocation Density and the Particle Size of Barium Oxide (BaO) Nanoparticle, Ibn AL-Haitham Journal For Pure and Applied Sciences 37(2) (2024) 195-204.

[18] M.K. Abood, M.A. Fayad, H.A. Al Salihi, H.A.A. Salbi, Effect of ZnO nanoparticles deposition on porous silicon solar cell, Materials Today: Proceedings 42 (2021) 2935-2940.

[19] J.-W. Zha, M.-S. Zheng, B.-H. Fan, Z.-M. Dang, Polymer-based dielectrics with high permittivity for electric energy storage: A review, Nano Energy 89 (2021) 106438.

[20] Y. Qi, S.M. Anlage, H. Zheng, R. Ramesh, Local dielectric measurements of $BaTiO_3$–$CoFe_2O_4$ nanocomposites through microwave microscopy, Journal of materials research 22(5) (2007) 1193-1199.

[21] A. Soleimani, M. Keshavarz, M.D. Chermahini, M.R. Saeri, M.R. Nilforoushan, Development of the magnetodielectric properties of $BaTiO_3$-$CoFe_2O_4$ multiferroic composites, Ceramics International 51(2) (2025) 1690-1698.

[22] A. Manjeera, M. Vittal, V. Reddy, G. Prasad, G. Kumar, Synthesis and characterization of $BaTiO_3$-$CoFe_2O_4$ composites, Ferroelectrics 519(1) (2017) 15-22.

[23] S. Halder, S. Bhuyan, R. Choudhary, Structural, dielectric and electrical characteristics of lead-free electro-ceramic: Bi ($Ni_{2/3}Ta_{1/3}$) O_3, Engineering Science and Technology, an International Journal 22(1) (2019) 376-384.

[24] M.E. Hajlaoui, R. Dhahri, N. Hnainia, A. Benchaabane, E. Dhahri, K. Khirouni, Conductivity and giant permittivity study of $Zn_{0.5}Ni_{0.5}Fe_2O_4$ spinel ferrite as a function of frequency and temperature, RSC advances 9(56) (2019) 32395-32402.

[25] S. Ahmed, S.K. Barik, S. Hajra, Investigation of electric, dielectric, and magnetic properties of Li^{+1} and Mo^{+6} co-doped $BiFeO_3$, Applied Physics A 125(5) (2019) 303.

[26] E. Şenarslan, M. Sağlam, Voltage-frequency dependence of the complex dielectric and electric modulus and the determination of the interface-state density distribution from the capacitance-frequency measurements of Al/p-Si/Al and Al/V2O5/p-Si/Al structures, Applied Physics A 130(9) (2024) 641.

[27] J. Jose, J.A. Salam, V. Thomas, Effect of temperature and frequency on the dielectric behaviour of cellulose nanocrystals, Industrial Crops and Products 222 (2024) 119428.

[28] Y. Wong, J. Hassan, M. Hashim, Dielectric properties, impedance analysis and modulus behavior of $CaTiO_3$ ceramic prepared by solid state reaction, Journal of alloys and compounds 571 (2013) 138-144.

[29] M. Ganaie, M. Zulfequar, Ac Conductivity Measurement of $Cd_5Se_{95-x}Zn_x$ Chalcogenide Semiconductor Using Correlated Barrier Hopping Model, Acta Physica Polonica A 128(1) (2015) 59-63.

[30] P. Vineetha, R. Jose, K.V. Saravanan, Effect of ZnO on (ferroelectric) fatigue retention and thermal stability of ferroelectric properties in lead free $(K_{0.5}Na_{0.5})(Nb_{0.7}Ta_{0.3})O_3$ ceramics, RSC advances 9(60) (2019) 34888-34895.

[31] V. Boddu, F. Endres, P. Steinmann, Molecular dynamics study of ferroelectric domain nucleation and domain switching dynamics, Scientific reports 7(1) (2017) 806.

[32] C. Feng, T. Liu, X. Bu, S. Huang, Enhanced ferroelectric, dielectric properties of Fe-doped PMN-PT thin films, Nanomaterials 11(11) (2021) 3043.

[33] A. Ali, A.E. Hannora, M. El-Desoky, A.E. Harby, Multifunctional Ferroelectric–Ferromagnetic behavior and high energy storage density in ball-milled nanostructured $KNbO_3$–Bi_2O_3–Fe_2O_3 for capacitive energy storage, Materials Science in Semiconductor Processing 207 (2026) 110497.

[34] S. Merselmiz, Z. Hanani, D. Mezzane, M. Spreitzer, A. Bradeško, D. Fabijan, D. Vengust, M.B. Amjoud, L. Hajji, Z. Abkhar, High energy storage efficiency and large electrocaloric effect in lead-free $BaTi_{0.89}Sn_{0.11}O_3$ ceramic, Ceramics International 46(15) (2020) 23867-23876.

[35] B. Wen, Y. Zhang, X. Liu, L. Ma, X. Wang, Temperature-dependent ferroelectric hysteresis properties of modified lead zirconate titanate ceramics, Journal of Materials Science 47(10) (2012) 4299-4304.

[36] C. Li, T. Zheng, J. Wu, Competitive mechanism of temperature-dependent electrical properties in $BiFeO_3$-$BaTiO_3$ ferroelectrics controlled by domain evolution, Acta Materialia 206 (2021) 116601.

[37] G. Wang, Z. Lu, Y. Li, L. Li, H. Ji, A. Feteira, D. Zhou, D. Wang, S. Zhang, I.M. Reaney, Electroceramics for high-energy density capacitors: current status and future perspectives, Chemical Reviews 121(10) (2021) 6124-6172.

[38] S. Li, T. Hu, H. Nie, Z. Fu, C. Xu, F. Xu, G. Wang, X. Dong, Giant energy density and high efficiency achieved in silver niobate-based lead-free antiferroelectric ceramic capacitors via domain engineering, Energy Storage Materials 34 (2021) 417-426.

[39] M. Atif, S. Ahmed, M. Nadeem, M.K. Ali, M. Idrees, R. Grössinger, R.S. Turtelli, Role of competing phases in the structural, magnetic and dielectric relaxation for $(1-x)\ CoFe_2O_4 + (x)\ BaTiO_3$ composites, Ceramics International 42(13) (2016) 14618-14626.

[40] A. Ponce, E. Chagas, R. Prado, C. Fernandes, A. Terezo, E. Baggio-Saitovitch, High coercivity induced by mechanical milling in cobalt ferrite powders, Journal of Magnetism and Magnetic Materials 344 (2013) 182-187.

[41] S. Xu, Y. Ma, B. Geng, X. Sun, M. Wang, The remanence ratio in $CoFe_2O_4$ nanoparticles with approximate single-domain sizes, Nanoscale Research Letters 11(1) (2016) 471.

[42] S. Amiri, H. Shokrollahi, The role of cobalt ferrite magnetic nanoparticles in medical science, Materials Science and Engineering: C 33(1) (2013) 1-8.

[43] A. Omelyanchik, M. Salvador, F. D'orazio, V. Mameli, C. Cannas, D. Fiorani, A. Musinu, M. Rivas, V. Rodionova, G. Varvaro, Magnetocrystalline and surface anisotropy in $cofe_2o_4$ nanoparticles, Nanomaterials 10(7) (2020) 1288.

[44] E. Almutib, M. Shariq, Y. Alqurashi, R. Karmouch, K. Alshehri, M. Sharma, K. Hassan, Y. Slimani, T. Zelai, A.A. Alamri, Exploring magnetic field-dependent super capacitive properties of $CoFe_2O_4$ nano blades for energy storage, Journal of Energy Storage 107 (2025) 114994.

[45] M. Shariq, A. Alzahrani, E. Almutib, A.F. Alharbi, S.A. Algarni, M.Y. Almashnowi, S.M. Bouzgarrou, W.A. Ghaly, S.K. Ali, K. Hassan, Harnessing the potential of $NiMn_2O_4$ nanoparticle: a next-generation supercapacitor electrode material, Physica Scripta 99(3) (2024) 035941.

[46] K. Purushothaman, B. Sethuraman, J. Johnson William, B. Saravanakumar, A novel $CoFe_2O_4/ZrO_2$/rGO ternary nanocomposite for high performance supercapacitor, Journal of Energy Storage 163 (2026) 122073.

[47] M. Libber, N. Gariya, M. Kumar, A comprehensive analysis of supercapacitors with current limitations and emerging trends in research, Journal of Solid State Electrochemistry 29(2) (2025) 513-527.

[48] N. Wally, E. Sheha, I.M. Morad, M.M. El-Desoky, Combined Effects of LiCl Addition and Solvent-in-Water Approaches on Aqueous Magnesium-Ion Battery Performance, ACS Applied Energy Materials 8(7) (2025) 4441-4455.

[49] H.M. Abd El-khabeer, K.F. Qasim, M.M. El-Kholy, M. El-Desoky, Dopant's coordination number impact on double phase formation of nanospherical ZnS, and its contribution in structural and electrochemical storage's mechanism for solid state electrolyte system, Journal of Alloys and Compounds (2026) 189714.

[50] N. Sinan Tatli, M. Yilmaz, E. Unur Yilmaz, Self-Activated SiO_2/C Nanocomposite from Silica-Rich Marine Mucilage for Supercapacitor Applications, ECS Advances 2(2) (2023) 020501.

[51] S.W. Tong, D.C.J. Neo, W.P. Goh, C. Jiang, Stable Metal-Organic Framework Based Electrode For Electrochemical Applications, 2022 IEEE 12th International Conference Nanomaterials: Applications & Properties (NAP), IEEE, 2022, pp. 1-4.

[52] J. Wang, F. Zheng, M. Li, J. Wang, D. Jia, X. Mao, P. Hu, Q. Zhen, Y. Yu, V_2O_5@ RuO_2 core–shell heterojunction nano-arrays as electrode material for supercapacitors, Chemical Engineering Journal 446 (2022) 136922.

[53] S. Sharifi, K. Rahimi, A. Yazdani, Largely enhanced pseudocapacitance by a facile in-situ decoration of MoS_2 nanosheets with $CoFe_2O_4$ nanoparticles, Journal of Energy Storage 72 (2023) 108499.

[54] M. Zhang, F. Zhao, Y. Yang, T. An, W. Qu, H. Li, J. Zhang, N. Li, Catalytic activity of ferrates ($NiFe_2O_4$, $ZnFe_2O_4$ and $CoFe_2O_4$) on the thermal decomposition of ammonium perchlorate, Propellants, Explosives, Pyrotechnics 45(3) (2020) 463-471.

[55] H.S. Magar, A. Mansour, A.B.A. Hammad, Advancing energy storage and supercapacitor applications through the development of Li^+-doped $MgTiO_3$ perovskite nano-ceramics, Scientific Reports 14(1) (2024) 1849.

[56] T. Zhao, L. Salamanca-Riba, H. Zheng, J. Wang, S. Lofland, Z. Ma, L. Mohaddes-Ardabili, S. Shinde, S. Ogale, F. Bai, Multiferroic $BaTiO_3$-$CoFe_2O_4$ nanostructures, (2004).

[57] S. Shankar, M. Kumar, V. Tuli, O. Thakur, M. Jayasimhadri, Energy storage and magnetoelectric coupling in ferroelectric–ferrite composites, Journal of Materials Science: Materials in Electronics 29(21) (2018) 18352-18357.

[58] D. Padmapriya, D. Dhayanithi, A. Rashid, M. Rahul, N. Kalarikkal, M. Muneeswaran, N. Giridharan, Composition-dependent structural, electrical, magnetic and magnetoelectric properties of (1− x) $BaTiO_3$− x $CoFe_2O_4$ particulate composites, Bulletin of Materials Science 43(1) (2020) 276.

[59] M. Chauhan, A. Agarwal, S. Sanghi, E. Arya, V. Vermani, A. Jangra, S. Kaushik, Crystal structure, dielectric and magnetic properties of $BaTiO_3$–$CoFe_2O_4$ magneto-electric composites, Materials Today: Proceedings 82 (2023) 186-191.

[60] L. Zia, G.H. Jaffari, J. Ricardo, A. Harvey, P.K.J. Wong, I. Shah, Correlation between the multiferroic properties in (1-x) $BaTiO_3$-x $CoFe_2O_4$ composites, Journal of Materials Science 59(48) (2024) 22149-22165.

[61] Y. Yoon, G. Jeong, J. Kim, H. Kim, S.H. Han, Y.-M. Kang, D.H. Kim, Ferroelectric, magnetic, and magnetoelectric properties of $BaTiO_3$–$CoFe_2O_4$ composites, Applied Physics A 132(5) (2026) 370.

Figure captions

Fig. 1: XRD pattern for the BTO-CFO sample.

Fig. 2(a): HR-TEM of BTO-CFO sample, **(b):** particle size distribution histogram, **(c):** lattice fringes with d spacing and **(d):** SAED pattern.

Fig. 3(a): Temperature dependence of real part for dielectric constant at different frequencies and **(b):** Temperature dependence of imaginary part for dielectric constant at different frequencies for the BTO-CFO sample.

Fig. 4: Frequency-dependence of real ε' for BTO-CFO sample at different temperatures.

Fig. 5: Frequency-dependence of σ_{ac} at 8 different temperatures. **Inset:** Exponent (s) versus temperature for the BTO-CFO sample.

Fig. 6: P-E hysteresis loops at four applied voltages at room temperature for the BTO-CFO sample.

Fig. 7: P-E hysteresis loops at five different temperatures at V = 220 volt for the BTO-CFO sample.

Fig. 8(a): P_{max}, P_r & E_c with temperature, **(b):** Temperature-dependence of the backswitching polarization and **(c):** Plot of ln (P_{max} - P_r) against reciprocal temperature at V = 220 volt for the BTO-CFO sample.

Fig. 9(a): Schematic diagram illustrations a typical P–E loop, **(b):** Hysteresis loop area <A> against temperature at V = 220 volt and **(c):** Energy storage efficiency and density at temperature range (298 K – 473 K) for the BTO-CFO sample.

Fig. 10: (M-H) loop for the BTO-CFO sample.

Fig. 11(a): CV at different scan rates and **(b):** log peak current vs. log scan rate for the BTO-CFO sample.

Fig. 12(a): GCD at different current densities, **(b):** Specific capacitance vs. current density relation, **(c):** Energy density vs. power density and **(d):** Capacity retention vs. the cycle number for the BTO-CFO sample.

Fig. 13: Nyquist plot of supercapacitor for the BTO-CFO sample.

Table. 1: Parameters obtained from EIS measurements.

Sample	$R_\circ$ (Ω)	CPE_1 ($F.s^{(\alpha-1)}$)	R_1 (Ω)	CPE_2 ($F.s^{(\alpha-1)}$)	R_2 (Ω)
BTO-CFO	42.15	$0.735x10^{-3}$	$0.12x10^{21}$	$12.71x10^{-6}$	183.7

Table. 2: Comparative with closely related studies.

Material / Study	Synthesis method	Structural phases	Dielectric / Ferroelectric properties	Magnetic properties	Energy-storage / Electrochemical performance	Main distinction from present work
Present BTO–CFO composite	Co-precipitation	$BaCoFe_6O_{11}$ (R-3m), $CoFe_2O_4$ (Fd-3m), $Ba_4Ti_2O_{27}$ (C2/m), BaO_2 (I4/mmm)	$\varepsilon' > 10^3$; TC ≈ 648 K; clear P–E hysteresis	Clear M–H hysteresis; Ms ≈ 7.8 emu g^{-1}	Cs = 288.8 F g^{-1} at 1 A g^{-1}; 211.1 F g^{-1} at 10 A g^{-1}; 90.3% retention/1000 cycles; W_r = 6.2 J cm^{-3}, η = 65.9%	Combines dielectric, ferroelectric, magnetic and electrochemical energy-storage properties in one composite
Zheng et al. [56]	Pulsed-laser deposition	BTO matrix + CFO nanopillars	Ferroelectric BTO; nanoscale FE/FM coupling	CFO nanopillars provide magnetic ordering	Not investigated	Pioneering demonstration of coupled FE/FM order in BTO–CFO nanostructures
Shankar et al. [57]	Solid-state reaction	Tetragonal BTO + CFO	P–E confirms ferroelectricity	Ferromagnetic CFO	W_r = 8.33 mJ cm^{-3}; η = 59.7% for BT–5CFO; ME coefficient = 13.33 mV cm^{-1} Oe^{-1}	Closest study concerning energy storage, but did not report supercapacitor/GCD performance.)
Wang et al. [4]	MOF-derived CFO + hydrothermal BTO	CFO + BTO	Ferroelectric behavior; magnetic field decreases P_r and E_c	CFO ferromagnetic	No electrochemical capacitance reported	Demonstrated strong interaction between BTO and CFO and magnetic-field-dependent ferroelectric properties.
Padmapriya et al. [58]	Solid-state reaction	Tetragonal BTO + cubic CFO	Dielectric and ferroelectric properties decrease with increasing CFO	M_s and M_r increase with CFO	Not investigated	Demonstrated composition-dependent FE/FM competition and ME coupling; maximum ME coefficient ≈ 17 mV cm^{-1} Oe^{-1}.

Material / Study	Synthesis method	Structural phases	Dielectric / Ferroelectric properties	Magnetic properties	Energy-storage / Electrochemical performance	Main distinction from present work
Chauhan et al. [59]	Solid-state reaction	Tetragonal BTO + cubic CFO	ε′/tanδ studied over 100 Hz–7 MHz and RT–573 K	M_r, M_s and μB increase with CFO	Not investigated	Confirmed two-phase BTO–CFO magnetodielectric behavior without additional phases.
Soleimani et al. [21]	Solid-state reaction	BTO + CFO; no impurity phases	At 7.5 wt% CFO: $\varepsilon_r \approx 2018$, $P_s \approx 12$ μC cm^{-2}, $P_r \approx 10$ μC cm^{-2}	M_s increased from 3.75 to 11.3 emu g^{-1} with CFO	No GCD/CV capacitance reported	Very close comparison: high dielectric constant and simultaneous FE/FM properties; however, the present work adds electrochemical energy storage.
Zia et al. [60]	Chemical synthesis + milling + SPS	Tetragonal BTO + cubic CFO	FE response mainly at low CFO; high CFO increases leakage	CFO clustering; magnetic response increases with CFO	Not reported	Shows that CFO content strongly controls the balance between ferroelectricity and magnetism.
Yoon et al. [61]	Solid-state reaction	BTO + CFO, no secondary phase	Polarization decreases with increasing CFO because of leakage	Saturation magnetization increases with CFO	Not investigated	Very recent direct BTO–CFO comparison; supports the coexistence of FE and magnetic responses but does not address electrochemical storage.

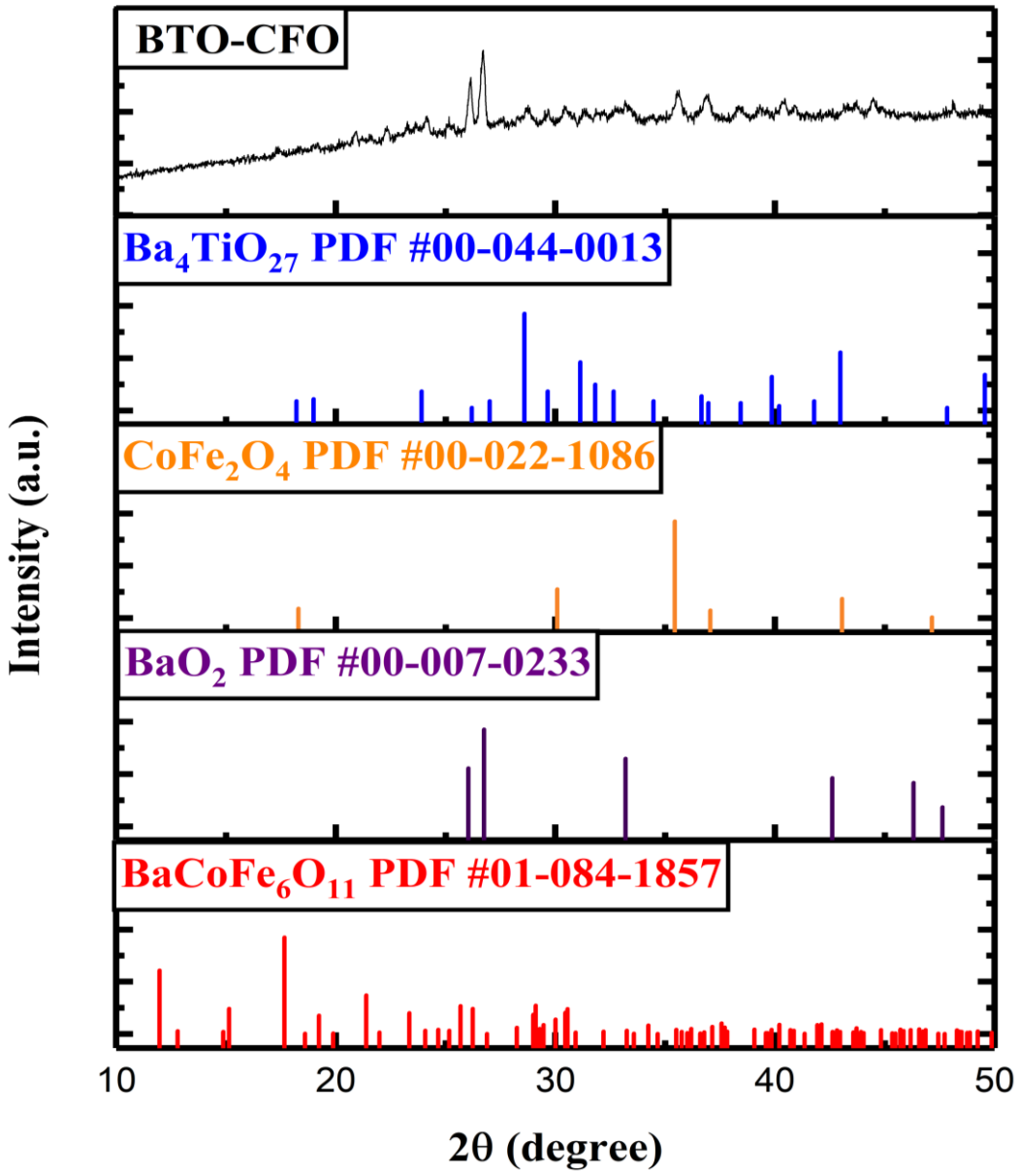
BTO-CFO
Ba4TiO27 PDF #00-044-0013
CoFe2O4 PDF #00-022-1086
BaO2 PDF #00-007-0233
BaCoFe6O11 PDF #01-084-1857
Intensity (a.u.)
10
20
30
40
50
2θ (degree)

Fig. 1

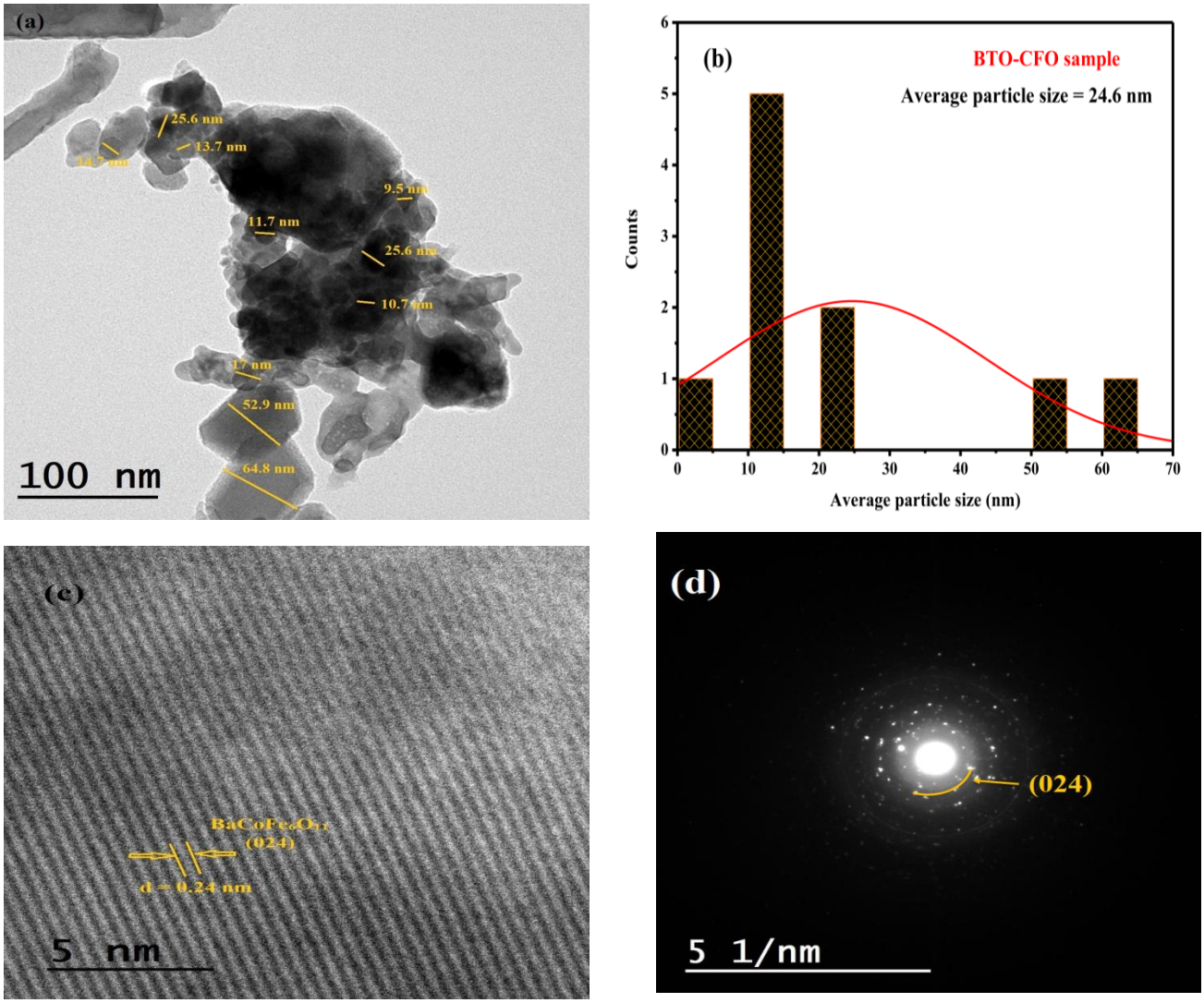
(a)
25.6 nm
13.7 nm
14.7 nm
9.5 nm
11.7 nm
25.6 nm
10.7 nm
17 nm
52.9 nm
64.8 nm
100 nm
(b)
BTO-CFO sample
Average particle size = 24.6 nm
Counts
Average particle size (nm)
0
10
20
30
40
50
60
70
1
2
3
4
5
6
(c)
BaCoFe6O11
(024)
d = 0.24 nm
5 nm
(d)
(024)
5 1/nm

Fig. 2

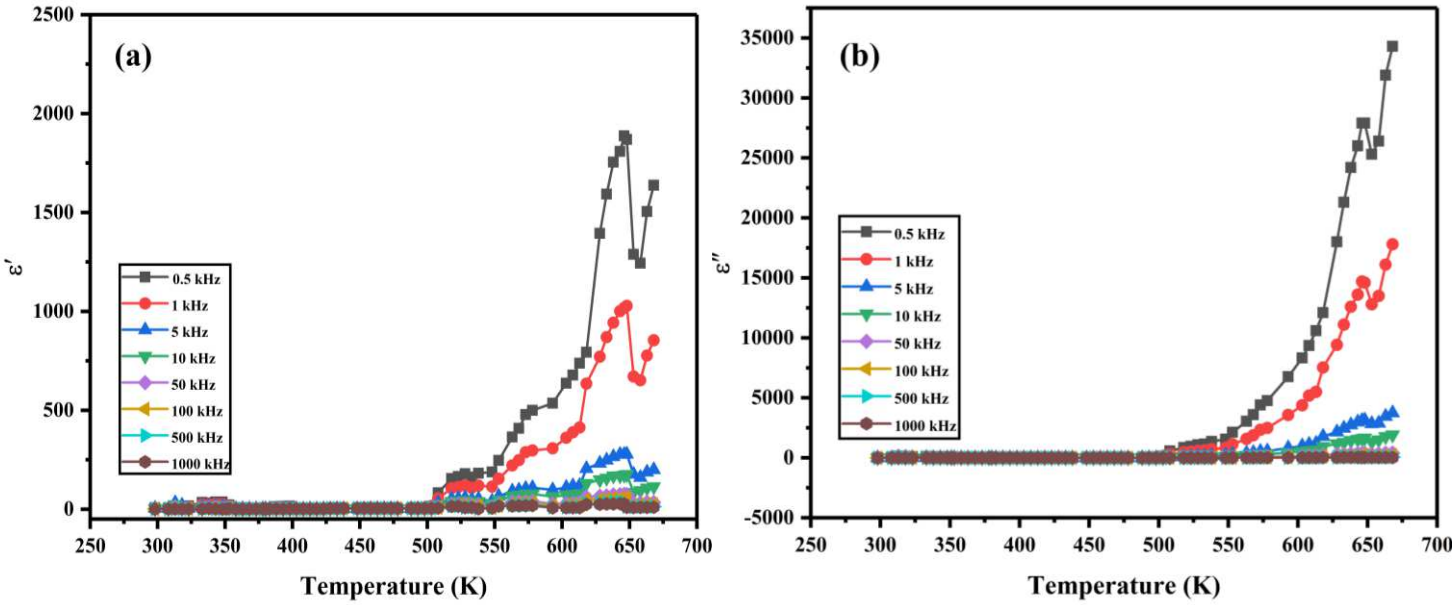
(a)
ε′
Temperature (K)
0.5 kHz
1 kHz
5 kHz
10 kHz
50 kHz
100 kHz
500 kHz
1000 kHz
(b)
ε″
Temperature (K)

Fig. 3

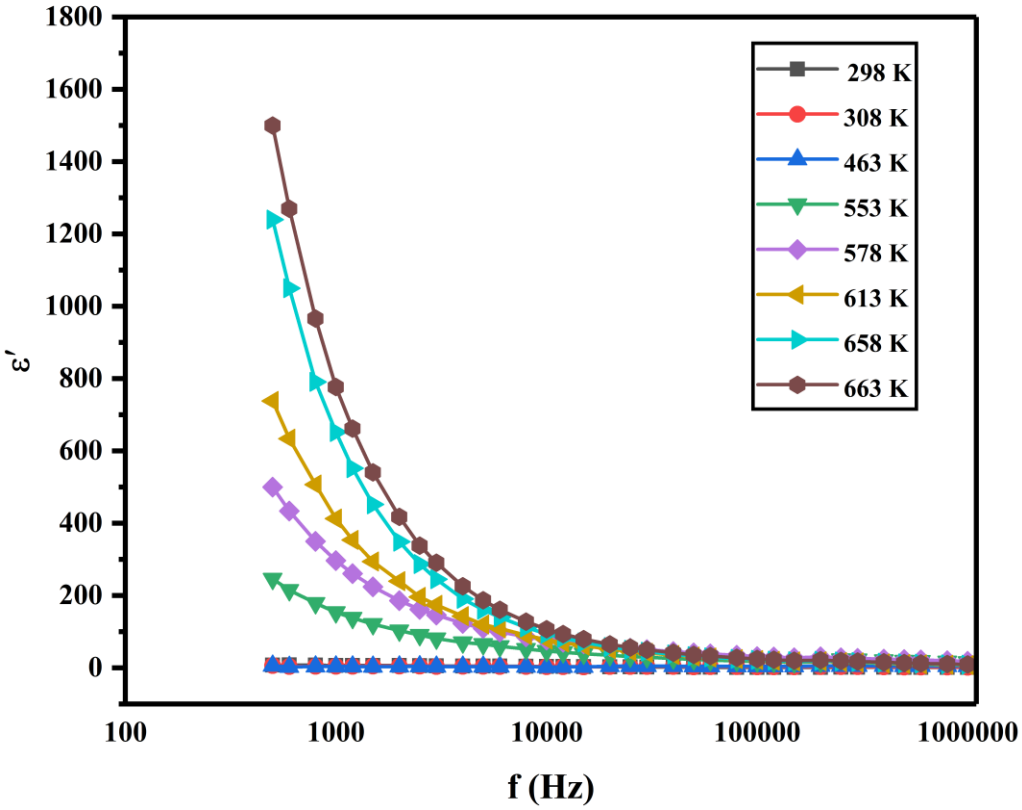
1800
1600
1400
1200
1000
800
600
400
200
0
ε′
100
1000
10000
100000
1000000
f (Hz)
298 K
308 K
463 K
553 K
578 K
613 K
658 K
663 K

Fig. 4

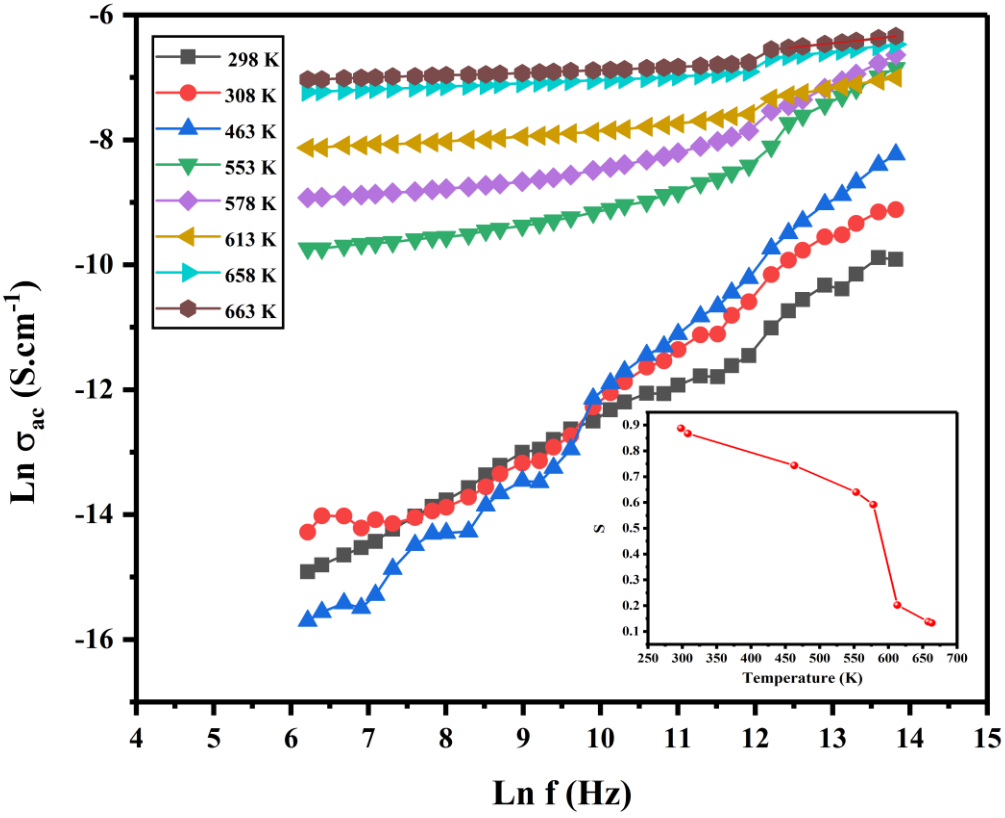
298 K
308 K
463 K
553 K
578 K
613 K
658 K
663 K
Ln σac (S.cm-1)
Ln f (Hz)
S
Temperature (K)

Fig. 5

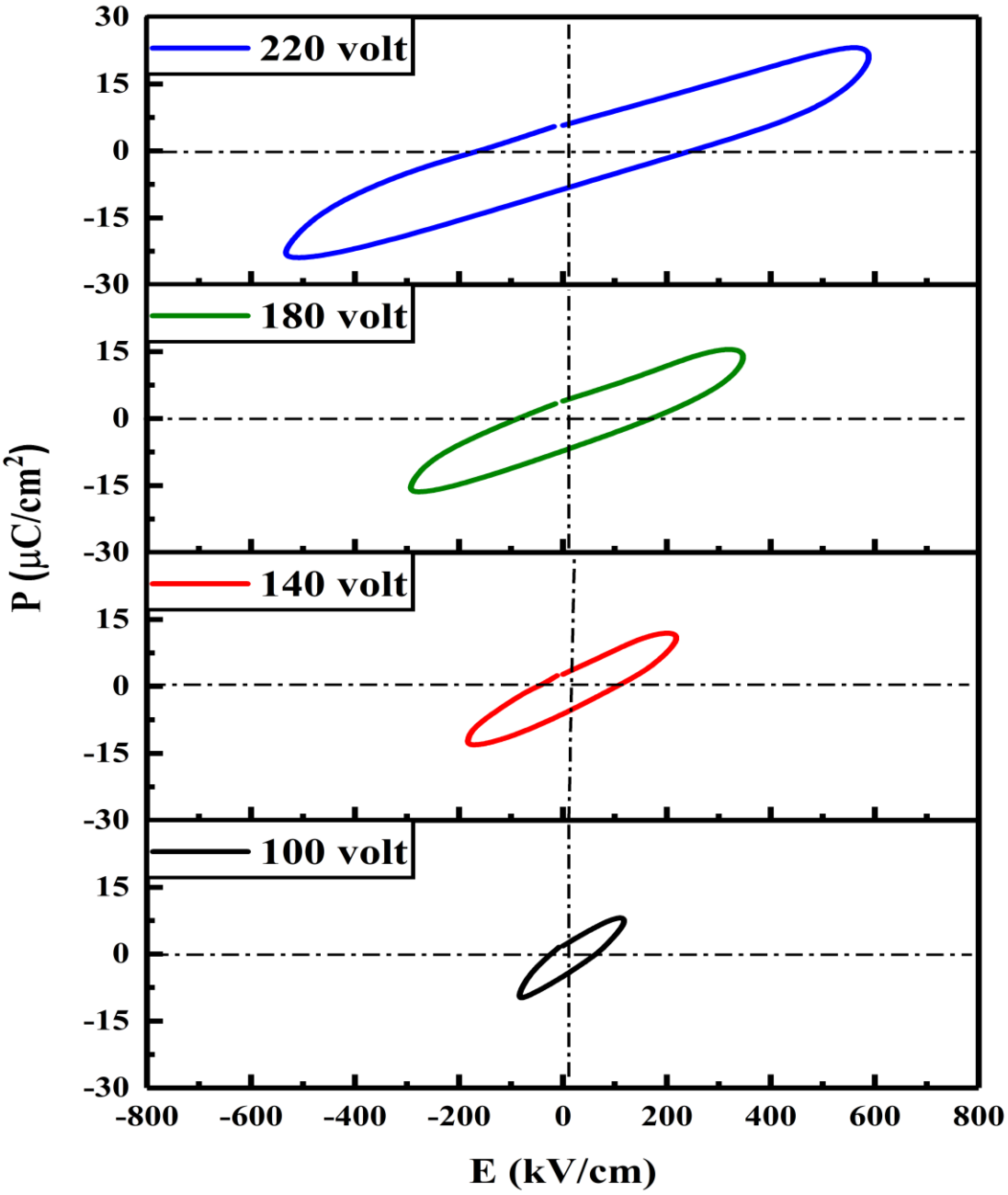
220 volt
180 volt
140 volt
100 volt
30
15
0
-15
-30
-800
-600
-400
-200
0
200
400
600
800
P (μC/cm²)
E (kV/cm)

Fig. 6

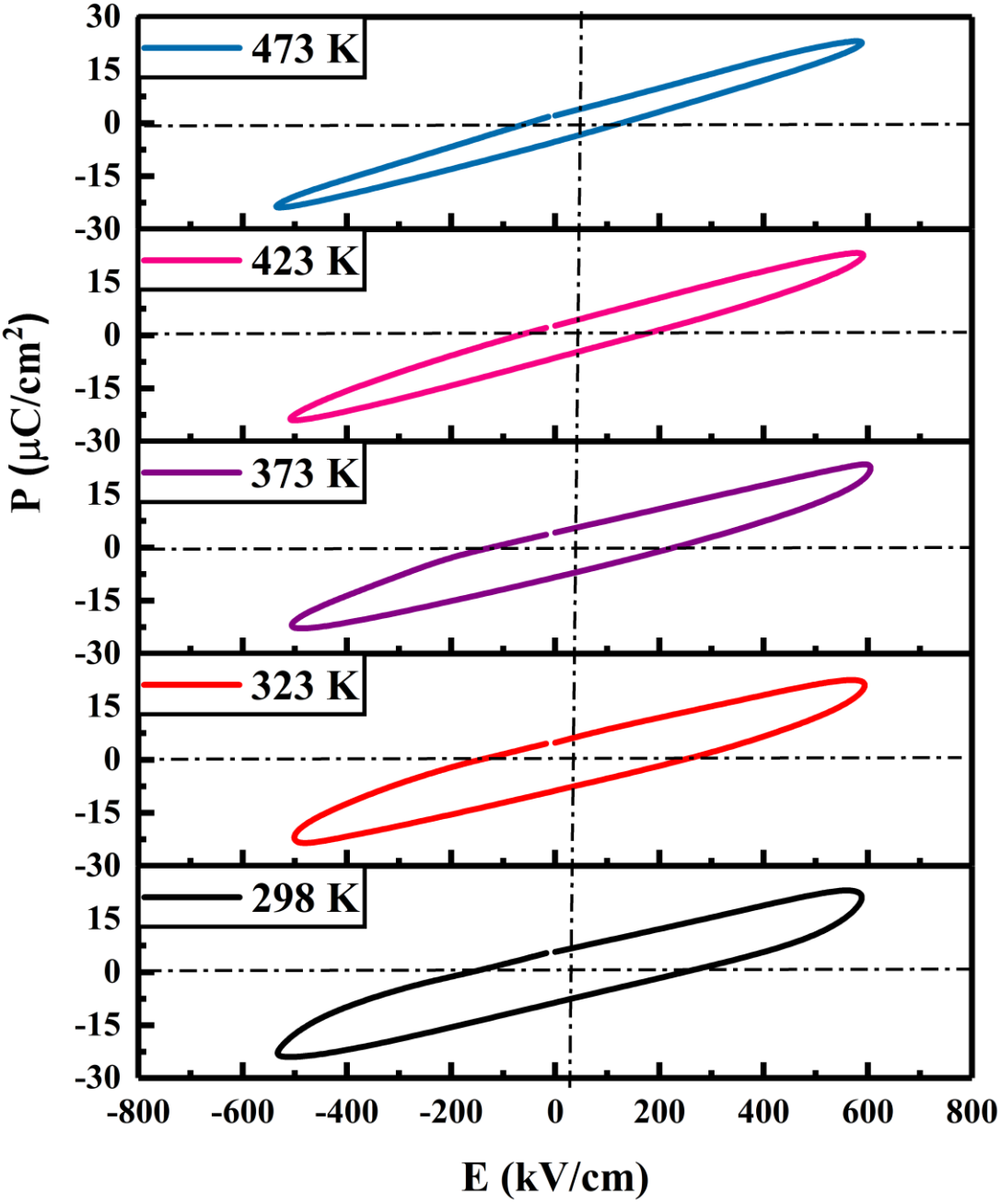
473 K
423 K
373 K
323 K
298 K
P (μC/cm²)
E (kV/cm)
30
15
0
-15
-30
-800
-600
-400
-200
0
200
400
600
800

Fig. 7

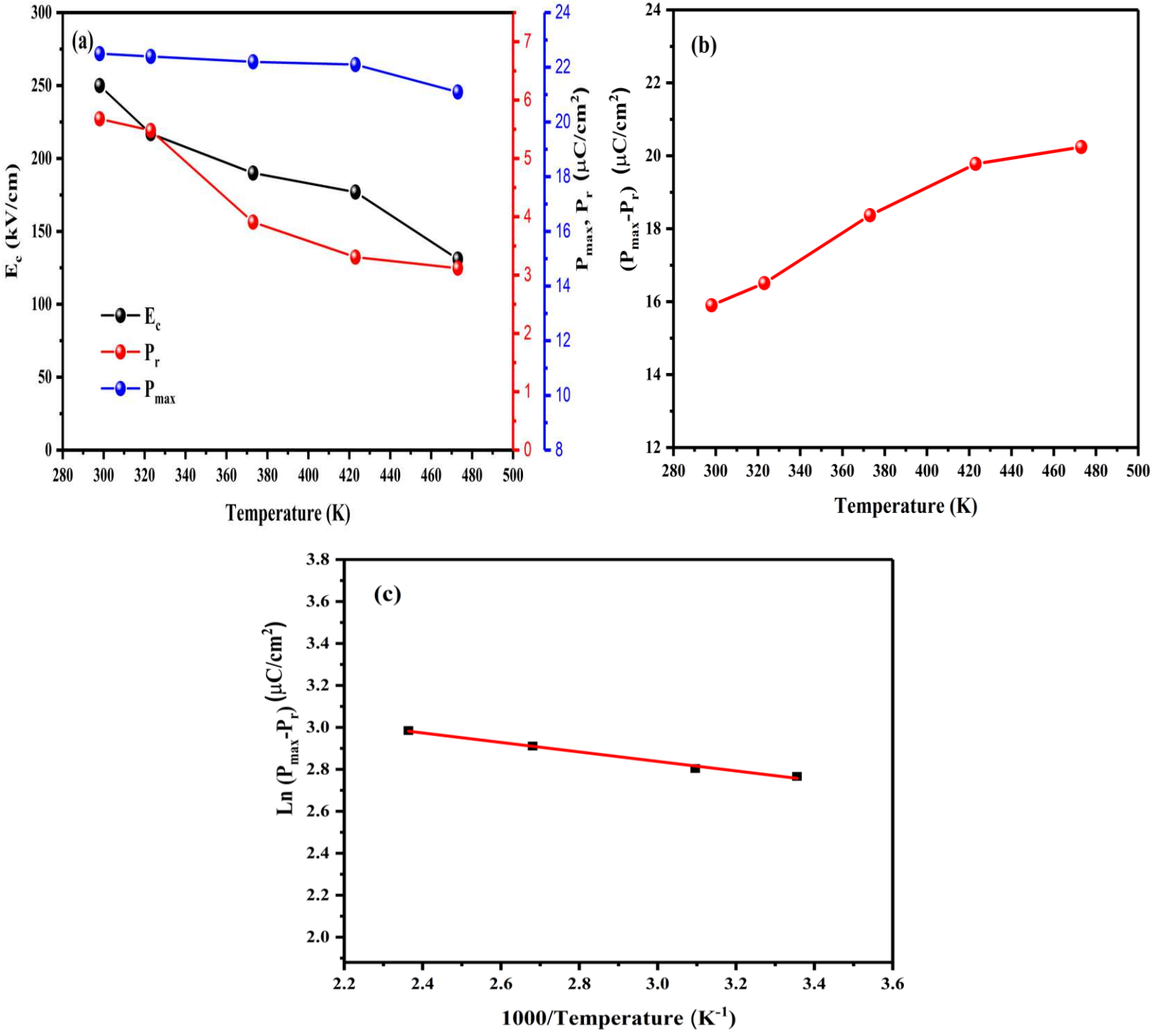
(a)
E_c (kV/cm)
P_{max}, P_r ($\mu C/cm^2$)
Temperature (K)
E_c
P_r
P_{max}
(b)
$(P_{max}-P_r)$ ($\mu C/cm^2$)
Temperature (K)
(c)
Ln $(P_{max}-P_r)$ ($\mu C/cm^2$)
1000/Temperature (K^{-1})

Fig. 8

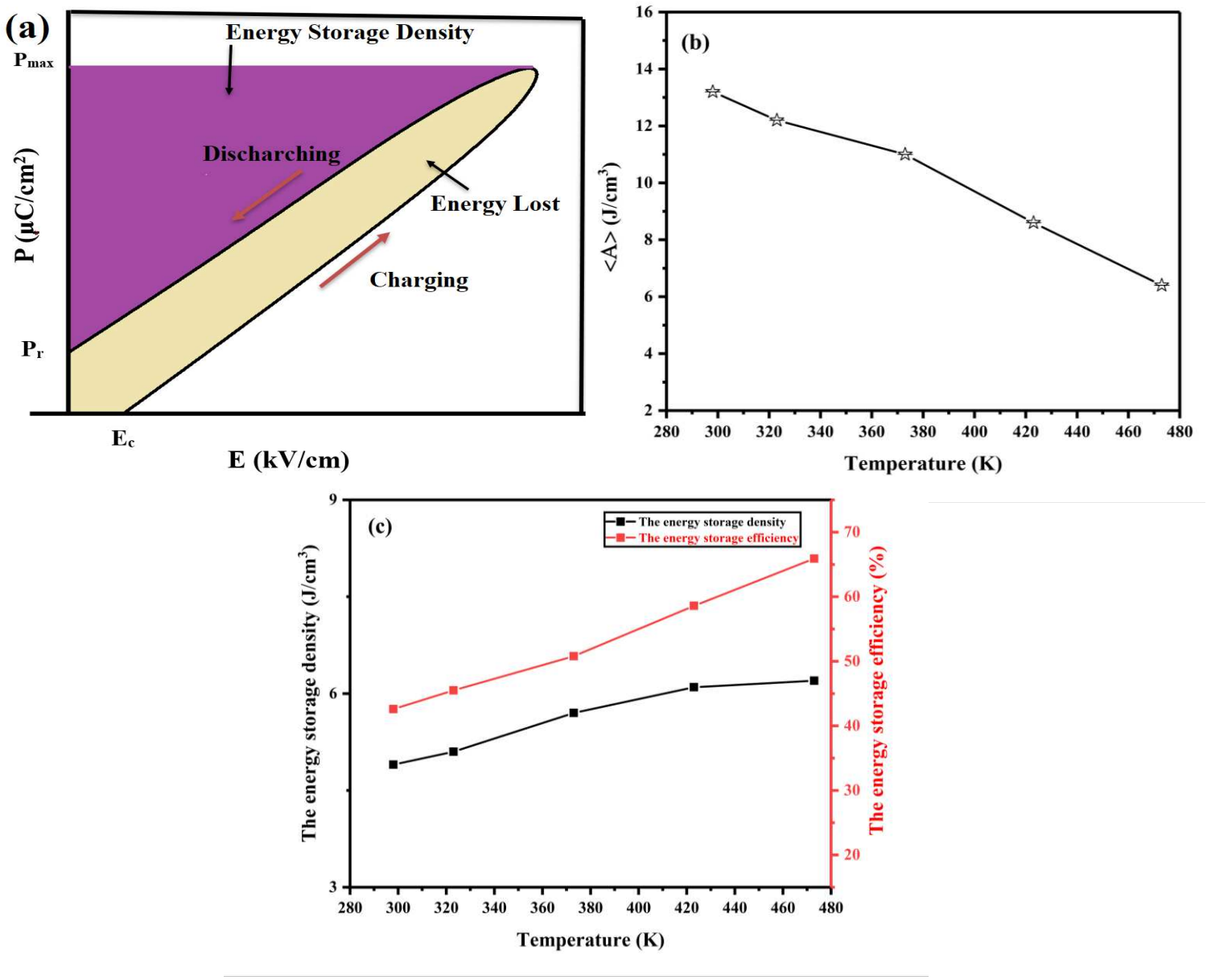
(a)
Energy Storage Density
Pmax
Discharching
Energy Lost
Charging
Pr
P (μC/cm²)
Ec
E (kV/cm)
(b)
<A> (J/cm³)
Temperature (K)
(c)
The energy storage density
The energy storage efficiency
The energy storage density (J/cm³)
The energy storage efficiency (%)
Temperature (K)

Fig. 9

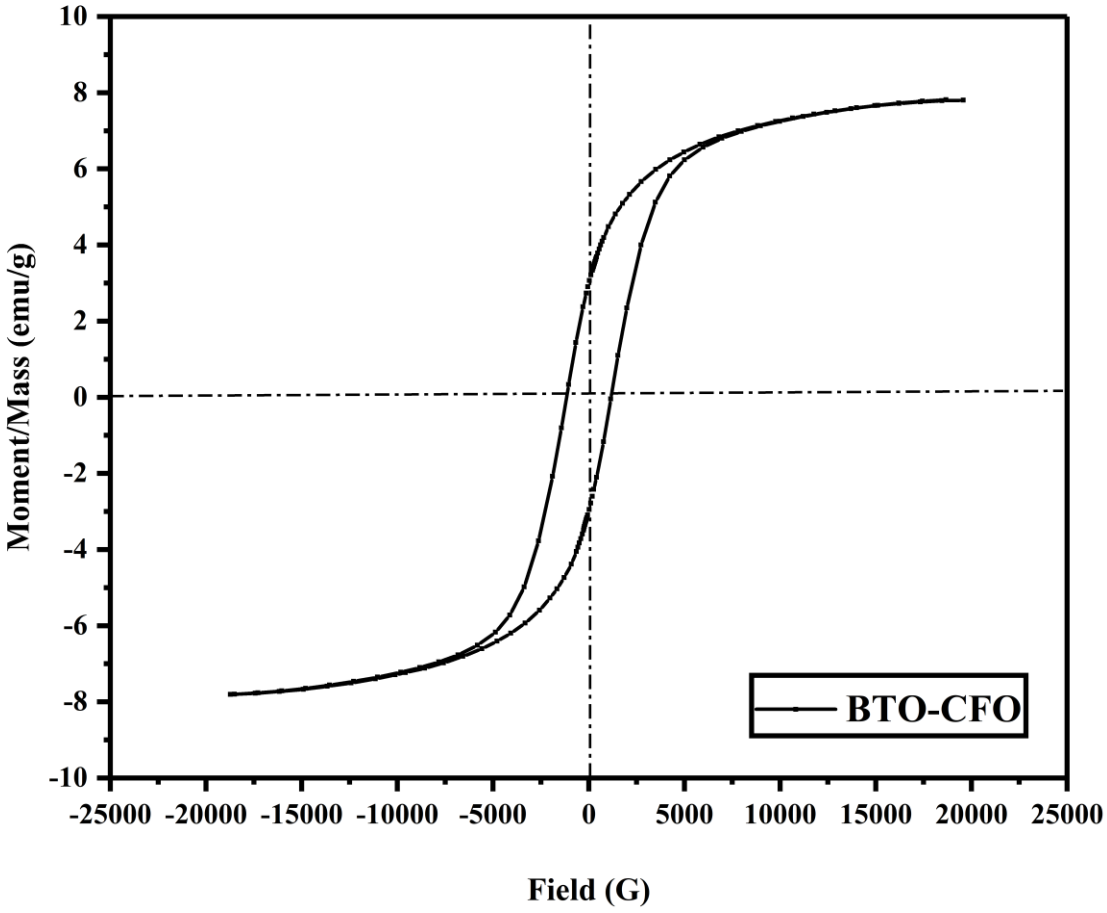
Moment/Mass (emu/g)
10
8
6
4
2
0
-2
-4
-6
-8
-10
-25000
-20000
-15000
-10000
-5000
0
5000
10000
15000
20000
25000
Field (G)
BTO-CFO

Fig. 10

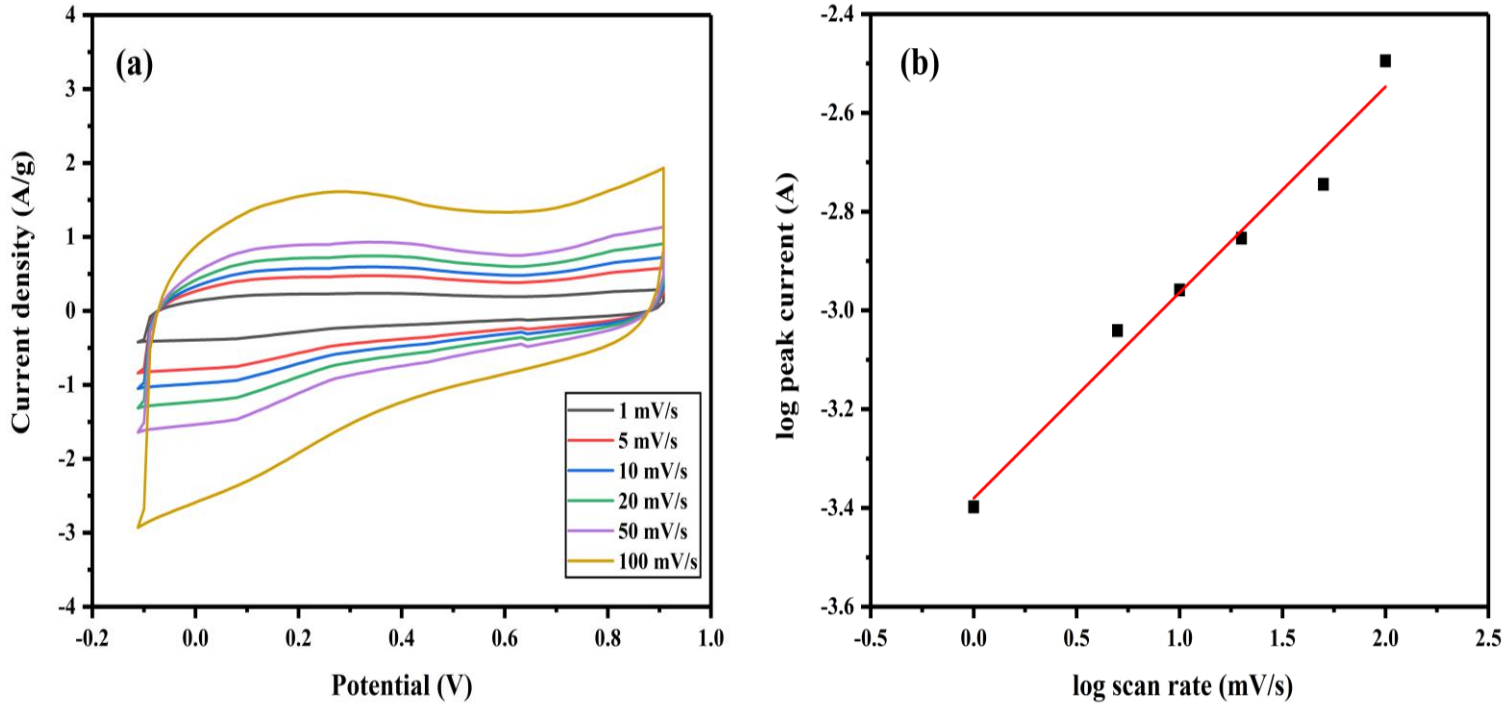
(a)
Current density (A/g)
Potential (V)
1 mV/s
5 mV/s
10 mV/s
20 mV/s
50 mV/s
100 mV/s
(b)
log peak current (A)
log scan rate (mV/s)

Fig. 11

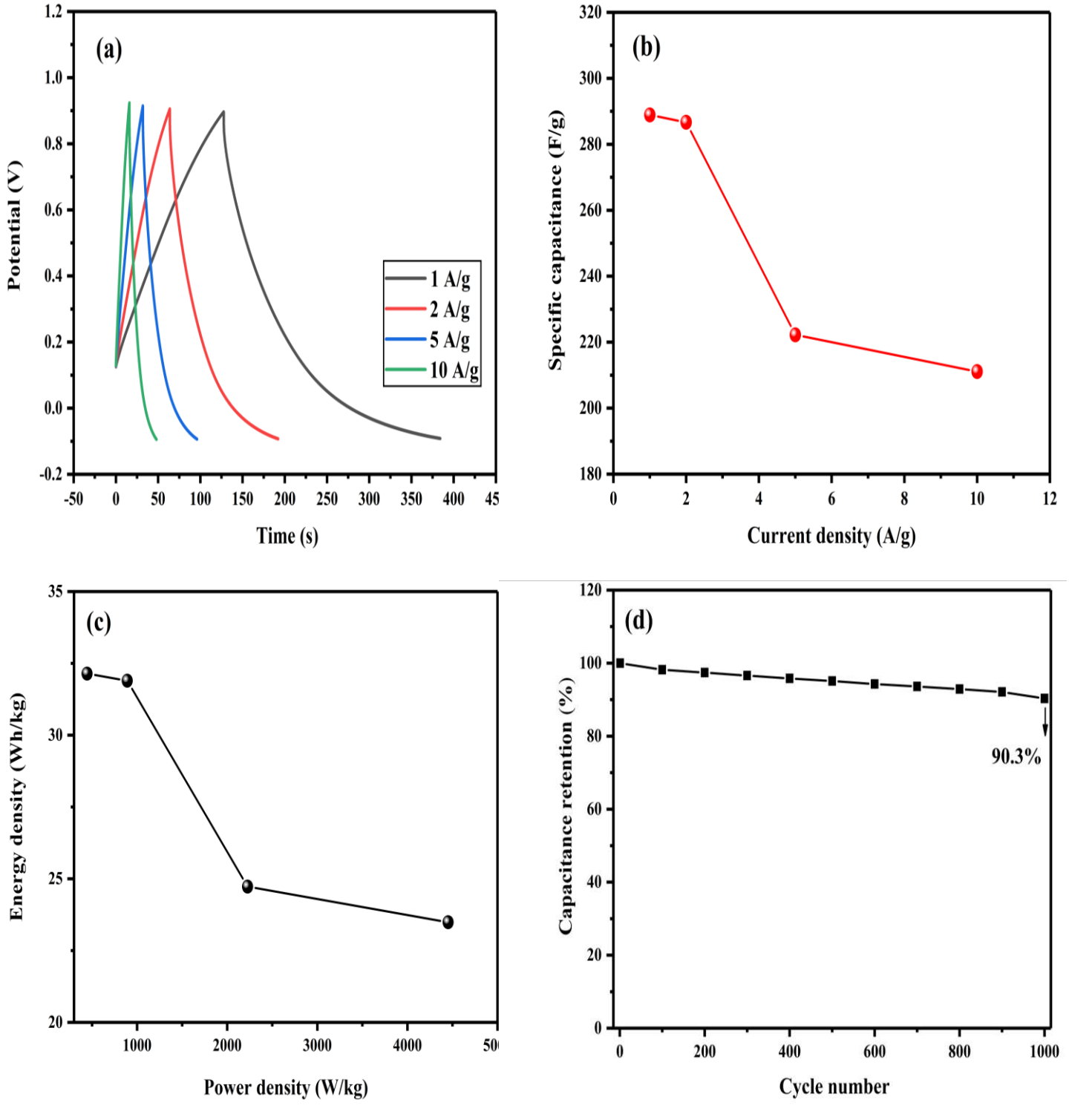
(a)
Potential (V)
Time (s)
1 A/g
2 A/g
5 A/g
10 A/g
(b)
Specific capacitance (F/g)
Current density (A/g)
(c)
Energy density (Wh/kg)
Power density (W/kg)
(d)
Capacitance retention (%)
Cycle number
90.3%

Fig. 12

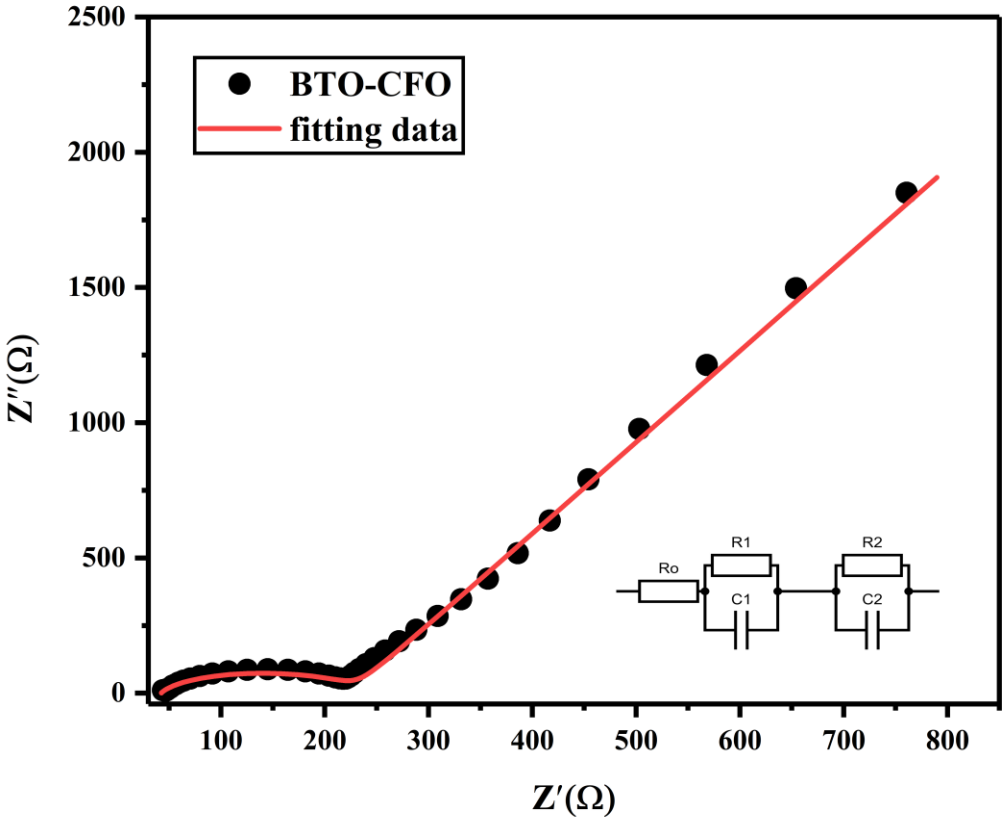
BTO-CFO
fitting data
Z″(Ω)
Z′(Ω)
2500
2000
1500
1000
500
0
100
200
300
400
500
600
700
800
Ro
R1
C1
R2
C2

Fig. 13